Pontificia Universidad Católica de Chile
Physics Department

Self-Assembly of Submonolayer-Coverage Organic Films

by

Tomás Patricio Corrales Iturriaga

Thesis presented to the Physics Faculty of the
Pontificia Universidad Catolica de Chile
in partial fulfillment of the requirements for the
degree of Master in Physics

Advisor : Dr. Ulrich G. Volkmann
Correction Committee : Dr. Alejandro Cabrera
Dr. Rafael Benguria

April, 2009
Santiago – Chile

To my family, girlfriend, school friends, advisor, professors and college mates...I deeply thank, you are all part of this work.

Acknowledgments

I would like thank my advisor Dr. Ulrich Volkmann and my laboratory mates: Edgardo Cisternas, Valeria del Campo, Carlos Calle, Pia Homm, Piero Ferrari, Pablo Morales, Ignacio Vergara, Fabian Olivares, Pamela Soza, Marcela Soto, Enrique Valderrama, Julio Valenzuela, Manuel Pino, Jonathan Avila, Marcelo Ruiz, Gonzalo Avaria, Felipe Veloso and Estaban Ramos-Moore.

I would also like to thank dear college friends of mine, such as Pia Amigo, Felipe Navarrete, Rodrigo Herrera, Fernando Guzman, Claudia Araya, Raul Santos, Pia Valdivia and my school friends: Eduardo Martinez, Nicolas Salvo, Roberto Jadue, Jorge Gaete, Samuel Rodriguez, Maximiliano Devoto, Joaquin Catalan, Andres Orellana, Jurgen Egger, Rodrigo Leppe, Camilo Ureta and Federico Szczaranski

Finally I would like to thank the financially support given by CONICYT throughout Project FONDECYT 1060628.

Abstract

In this work we present a study of self assembled submonolayer coverage organic films. The types of molecules studied here are n-alkane chains, mainly n-dotriacontane (n - $C_{32}H_{66}$), that are deposited on silicon substrates with a thin native silicon oxide layer ($\sim$ 15Å). In this research we have developed a velocity controlled dip-coating device to prepare submonolayer films. We have identified the parameters that affect the coverage, morphology and structures that arise in the preparation of the film.

The techniques used to characterize these films are Atomic Force Microscopy (AFM), Scanning Electron Microscopy (SEM) and Energy Dispersive Spectroscopy (EDS). Furthermore, this is the first work that demonstrates that SEM is a plausible technique to study thin films of n-alkanes. The future importance of this research is related to the possibility of micro-structuring energetically homogenous surfaces with nanometer thick films using relatively simple techniques, such as velocity controlled dip-coating. Micro-structured patterns, such as the stripes reported here, could be applied as optical diffraction grids or as templates for other materials.

Contents

List of Figures

Chapter 1

Introduction

Thin films have a wide range of applications in industrial processes, from the semiconductor industry to biological applications. In particular, organic films have been of great interest in today's actual research due to their self assembly properties and their diverse phase transitions.

In this work we shall present a study of films that self assemble in different submonolayer coverage structures. The organic films that are studied are made of *n*-dotriacontane ($C_{32}H_{66}$ or C32), and are grown on Si/SiO_2 surfaces. In this chapter we will review the molecules to be studied; their molecular ordering on silicon surfaces and the technique that we will implement to prepare these submonolayer-coverage films.

1.1 Organic Films

Organic compounds are common in our day to day life mainly because they are composed of two of the most abundant atoms in nature, carbon and hydrogen, and also due to their chemical affinity in forming covalent bonds. Molecules containing hydrogen and carbon can form diverse types of structures, such as linear molecules, ring type molecules or branched type structures. This is related to the fact that carbon atoms can form single, double or triple bonds between themselves and hydrogen atoms. Furthermore carbon and hydrogen structures are found to bind with other atoms such as oxygen (O), nitrogen (N), sulfur (S), chlorine (Cl), bromine (Br) and iodine (I) making

the list of organic based molecules even vaster [1]. The only main requirement for a compound to be classified as organic is the presence of hydrocarbon bonds, which is remarkable due to the overwhelming number of different characteristics and functionalities that an organic molecule can posses.

Organic based materials are naturally formed and found on Earth. Proteins, peptides and DNA strings are some important examples of naturally formed organic molecules. Furthermore, life as we know it, is based on organic materials and their physical study has given way to important discoveries in the field of biophysics. Despite of being naturally found on earth, organic materials have also been synthesized in laboratories, leading to diverse structures such as polymers, which are macromolecules formed of repeating units of hydrocarbon based monomers. The number of repeating units for a molecule to be defined as a polymer is such that the addition or substraction of a repeating unit does not affect profoundly the properties of the material [2]. Polymers have been of great importance in modern industrial applications, a good example is the use of rubbers and plastics.

The molecules that are presented in this work are the simplest organic compounds that can be studied; nevertheless, the complete understanding of their growth mechanisms, structure and phase transitions is of critical importance for the understanding of more complex molecules. These simple molecules are called Alkanes which are formed only by hydrocarbon single bonds, no other atoms are found in these molecules. An alkane molecule can also form diverse types of structures, from closed ring-type to linear structures (see fig.1.1)

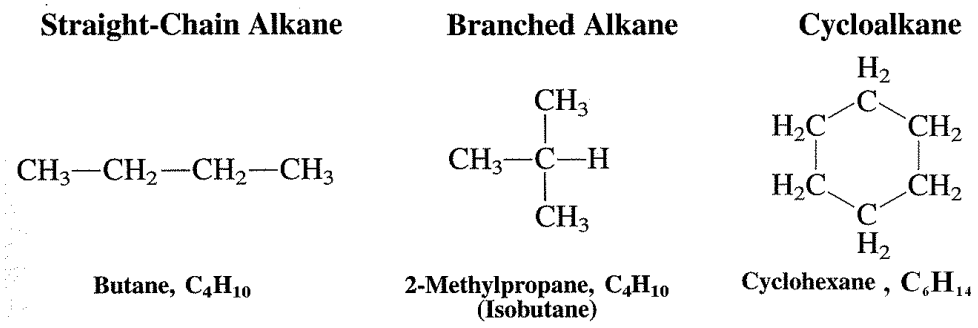

Figure 1.1: *Different types of alkane molecules (image from [1]).*

In particular, linear hydrocarbons, called n-alkanes are of interest because of their low chemical reactivity [1]. These linear molecules can be found in gas, liquid or solid states depending on the number of carbon atoms. At ambient temperatures (293 K), solid n-alkanes are commonly found in molecules with more than 20 carbon atoms and their bulk crystallization is due to intermolecular *van der Waals Forces*. The term van der Waals force is used today to describe collectively all intermolecular interactions. In particular n-alkanes are nonpolar molecules that crystalize by a type of *van der Waals* force called *London Force* which is due to electron correlation [1]. London forces are weak attractive forces that fall off as the sixth power of the distance between molecules, although for large distances this power law does not work well and was corrected by Polder and Casimir in 1948. A simple overview of these ideas can be found in [3]. It is found in Casimir's work that for large distances the attraction force actually falls like the seventh power for nonpolar atoms, however the London model works well for explaining the crystallization of n-alkanes which occurs at rather small atomic distances. This bonding force grows with the length of the n-alkane molecule therefore affecting the thermodynamics of the material i.e. the bulk melting point or the evaporation temperature of the material.

The systems that shall be studied here are composed of thin films of n-dotracontane, $C_{32}H_{66}$ or C32 (see fig. 1.2), adsorbed on silicon surfaces. These surfaces typically have a native oxide layer of $\sim$15Å.

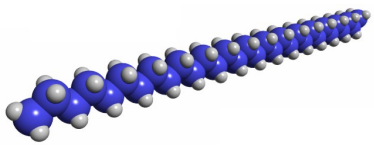

Figure 1.2: *n-$C_{32}H_{66}$ molecule.*

1.2 Dip-Coating

Dip-coating is a well known and widely used procedure to create thin films. This technique consists in submerging a substrate within a liquid and later withdrawing this substrate from the solution. In some cases the coating is formed while the substrate is submerged in the solution, while in other cases films are formed as the substrate is withdrawn from the solution. In this last case, thin films grow as the solvent evaporates leaving behind the coating.

In our experiments the volatile solvent that has been used for the past years is *n*-heptane (C_7H_{16} or C7) with solid bulk crystals of *n*-alkane disolved in it using a ultrasonic bath. The first version of dip-coating implemented in our laboratory consisted in completely submerging the substrate within the C7 solution and then quickly withdrawing it after some seconds within the solution. After this the substrate is placed on a piece of towel that rapidly absorbs the excess C7 leaving behind the film of *n*-alkane (see fig 1.3). It has been shown with ellipsometric measurements that organic films of n-alkane only grow when the heptane solution evaporates.

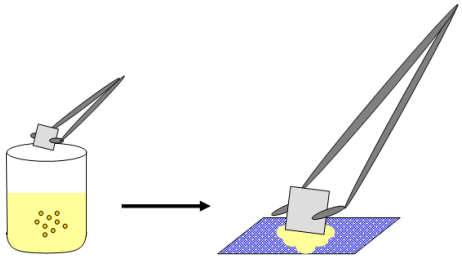

Figure 1.3: *Dip-Coating process initially used in our laboratory*

The substrates we use are made of silicon (Si) with a native layer of silicon oxide and are cleaned with a acid solution, known as piranha solution. This is a standard procedure to remove carbon based impurities off surfaces. This technique consists of a solution of sulfuric acid (H_2SO_4) with hydrogen peroxide (H_2O_2) heated at 90^0C in which the substrate is immersed for nearly half an hour. This cleaning procedure is one the most standard and efficient ways to clean silicon wafers obtaining with it reproducible hydrophobic clean surfaces[4].

The films that we have most intensively studied consists of C32 molecules. Molecular films grown with dip-coating have been study in the past with ellipsometry, atomic force microscopy and x-ray diffraction techniques [5],[6],[7], [8]. With these experiments it has been found that these films self assemble in multilayered structures consisting of 2 layers of molecules with their long axis parallel to the substrate (parallel bi-layer) followed by layers of molecules with their long axis perpendicular to the substrate (perpendicular layers) (see fig. 1.4). Furthermore, with our dip-coating procedure, samples present bulk particles which consists of many stacks of perpendicular layers with a depletion zone surrounding it. It is also found that the first perpendicular layer has a 2D rectangular crystal structure and that the parallel bilayer is most likely to be amorphous [10].

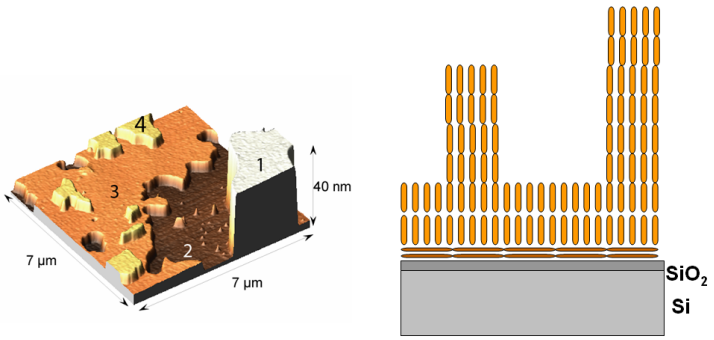

Figure 1.4: ***Left image****: AFM image from [5]. In this image a first and second perpendicular layers of ∼4 nm each appear (3), (4). Meanwhile (2) is a depletion zone were only parallel layers are believed to be found and (1) is a bulk or mesa shaped particle consisting of several perpendicular layer (∼ 50nm).* ***Right image****: Structure diagram of the layered film*

A further motivation to continue the study of dip-coating processes came from an investigation carried out by M. Bai *et al.* [9],[10],[11]. In this work it is shown that by slowly withdrawing the substrate from a solution of 20mL of C7 with less than 20mg of C32 disolved within, films with almost no bulk particles are grown. The films obtained with this method present no more than one perpendicular layer (∼ 4.2 nm)(see figs. 1.5. b) and c)) and do not form a complete monolayer, this is why we call them submonolayer coverage samples. The withdrawal velocity in these experiments is slow enough to allow the solvent to evaporate as the substrate is dragged, or pulled, out of the solution (fig. 1.5 a)).

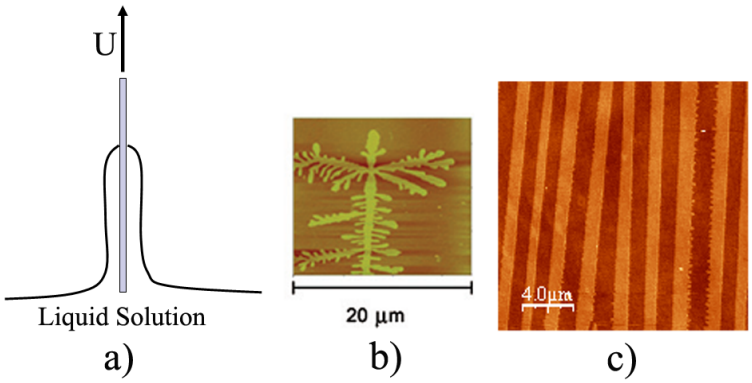

Figure 1.5: *a) The substrate is withdrawn vertically with a velocity U, low enough to allow the evaporation of solvent as the substrate is dragged out leaving an n-alkane film behind. b) AFM image after this dip-coating process. This morphology is referred to as a "Dragon Fly structure" (image from [10]) and presents only one perpendicular layer of molecules. c) Another AFM image (from [11]) after dip-coating with a different concentration of C32. These structures are referred to as stripes [11] and also present no more than one perpendicular layer.*

Although Bai *et al.* demonstrated that submonolayer coverage films with almost no bulk material can be obtained by slowly pulling the substrate from the solution, his experiments lacked of withdrawal velocity control. In fact, the withdrawal process was done manually in their experiments and the only variable they were able to vary systematically was the concentration of n-alkane (C32) disolved in the solvent (C7).

Even though there was no velocity control in M. Bai's experiments, some promising results were obtained, such as the one shown in figure 1.5.c). In this AFM image of $\sim 20x20\mu m^2$ microstructured stripes were observed. These stripes are separated by about 1 μm and are only one perpendicular layer thick ($\sim$ 4.2 nm). These stripes self assemble in a direction parallel to the pulling direction. According to reports by M. Bai, the solution required to prepare such films have a concentration of 15 mg of C32 disolved in 20 ml of C7.

Ordered aggregates of molecules such as fig.1.5.c) have a wide range of potential applications including novel optical, sensing and data recording platforms [12] [13], as well as templates for non-lithographic patterning. An important work in this direction came from M. Ghosh et. al [15] who managed to self assemble over a energetically homogeneous surface patterned stripes of film by vertically dip-coating gold coated silicon wafers with controlled withdrawal velocity (see fig. 1.6). The stripes found by M. Ghosh are formed perpendicular to the pulling direction, in contrast to the stipes found by M. Bai. These stripes are composed by spherical shaped particles of functionalized surfactant-free polystyrene amidine with diameters of 0.21 μm, 0.81 μm, 2.1 μm, instead of C32 molecules. These spheres were diluted in water forming a colloidal suspension.

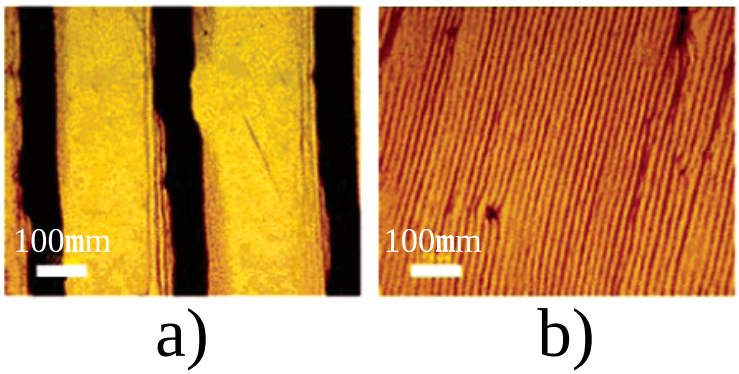

Figure 1.6: *Optical Micrographs of stripe patterns that form spontaneously on energetically homogeneous gold-coated silicon wafers at different withdrawal velocities for particles of 0.81 μm in diameter (images from [15]): a)10 μm/min b)200 μm/min*

M. Gosh's explained that as the substrate is pulled, the combined action of the plate velocity and the rapid evaporation near the three phase contact line convects particles towards this zone where they accumulate. They observe a clear dependence of velocity over the stripe formation and a critical velocity around 200μm/min where these stripes drastically narrow about an order of magnitud. The stripes described in their work were separated according to three distinct driving mechanisms or regimes (see fig. 1.7).

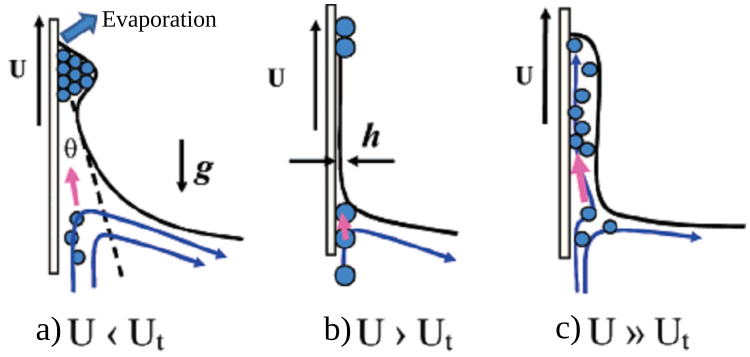

Figure 1.7: *Schematic representation of particle accumulation and flow pattern when a plate is removed from a suspension, from [15]. a) Gravity driven contact line jumping regime $U < U_t$: particles are convected by evaporative flux to the contact line. They pin the contact line at a finite contact angle. The meniscus is stretched by the plate motion. When it is too heavy, it tears off and jumps backward. b) Film entrainment regime $U > U_t$: A film of thickness h is entrained on the plate. Particles are to large to enter the film and accumulate to form a stripe roughly one particle high. The stripe eventually dries and a new three phase contact line forms. c) Transition to disorder $U >> U_t$: The entrained film is thick enough to convect particles freely into the film and deposit with no order.*

The central idea of the chapters to come is to implement a velocity controlled dip-coating experiment and to investigate the relationship between the morphology of the obtained films and the withdrawal velocity.

Chapter 2

Experimental Setups

In this chapter we will present the experimental setup used to prepare films with submonolayer coverage. The experimental setup has evolved in the course of this research from manual preparation of films to velocity controlled dip-coating. The first samples made are studied with Atomic Force Microscopy (AFM) operated in intermittent contact mode. Later, we realized that given that all samples have no more than one perpendicular layer, the important features to study are coverage and morphology. Given that our AFM has a maximum area scan of (30 x 30) μm^2, we turned to Scanning Electron Microscopy (SEM) and find that our samples are stable enough to resist high vacuum conditions needed for optimum SEM operation. Furthermore, this is the first work that demonstrates that SEM is a plausible technique to study thin films of n-alkanes.

In this chapter we will go through the experimental setup implemented to prepare samples with velocity controlled dip-coating. Also, we will present a quick overview of the main techniques that we use to characterize the samples, *i.e.* AFM and SEM.

2.1 Velocity Controlled Dip-Coating

The setup presented here is the final version of the velocity controlled dip-coating experiment that we have been developing throughout the course of this research. This setup mainly consists of a **unipolar stepper motor** that turns a 9 mm diameter gear wheel connected to a micrometer screw through a toothed belt. The micrometer screw has a diameter of 18 mm at the zone where it is attached to the toothed belt. Each whole turn of the micrometer screw is equivalent to a half a millimeter-linear movement, in the vertical direction, of the platform that the screw moves. The whole turn with the micrometer screw is separated in 50 divisions, this translates to a linear vertical movement of 10 μm per division. The optical platform that the micrometer screw controls has been adapted to move a tweezer in and out of the dip-coating solution (see fig 2.1).

The pulling velocity is controlled by the stepping frequency of the motor. It is measured that the displacement of the micrometer screw is ~ 10 μm for each step the motor takes. The reason why we choose a stepper motor, instead of a DC motor, is that the velocity and torque of a stepper motor are controlled independently. The stepping frequency is given by an **electronic control circuit**; meanwhile, the torque of the motor is controlled by an external power supply that regulates the power consumption of the motor windings. The range of velocities obtained with this setup ranges from 0.2 cm/min to 6 cm/min.

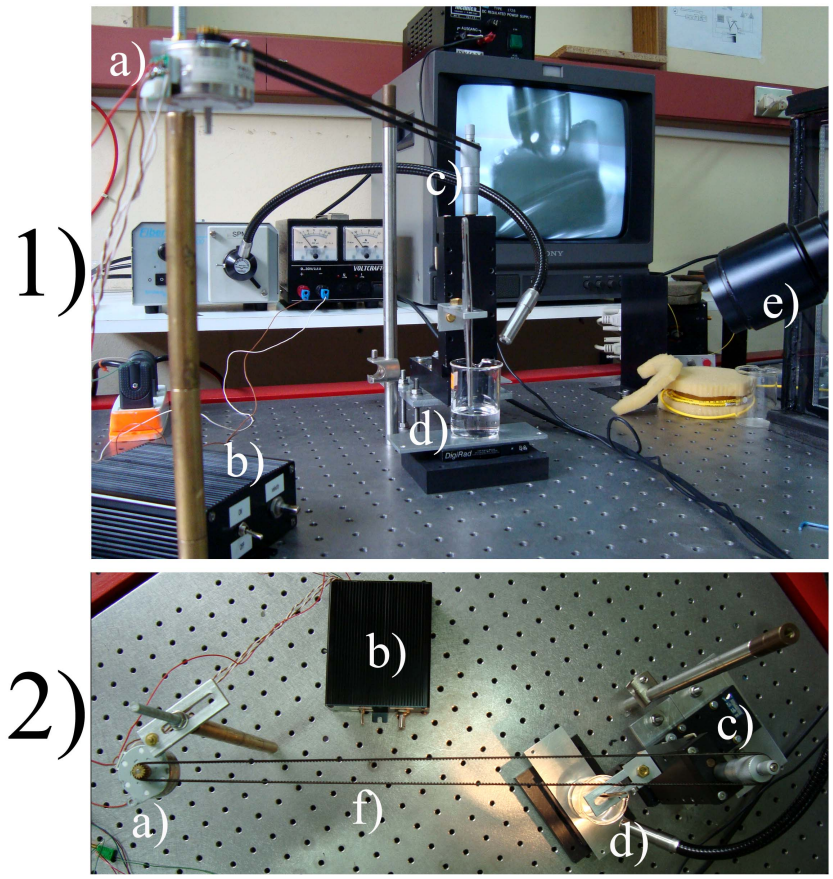

Figure 2.1: *Front (1) and top (2) view of the experimental setup. 1a) and 2a): Stepper motor. 1b) and 2b): Stepper electronic control circuit. 1c) and 2c): Micrometer screw. 1d) and 2d): Tweezer and dip-coating solution. 1e): CCD camera to observe air/solution interface (as seen on the TV screen in the back). The CCD camera is used to precisely lower the substrate without dipping the tweezers. Image 2f) shows the toothed belt connecting the motor with the micrometer screw.*

2.1.1 Stepper Motors

A stepper motor is an electromechanical device which converts electrical pulses into discrete mechanical movements. The shaft or spindle of a stepper motor rotates in discrete step increments when electrical command pulses are applied to it in the proper sequence. The motors rotation has several direct relations to these applied input pulses. For example the sequence of the applied pulses is directly related to the direction of

the motor shafts rotation; the speed of the motor shafts is connected to the frequency of the input pulses and the length of the rotation to the number of input pulses applied.

Some typical stepper motor designs are the Variable-Reluctance motor and the Permanent Magnet Motor (see fig. 2.2)[1].

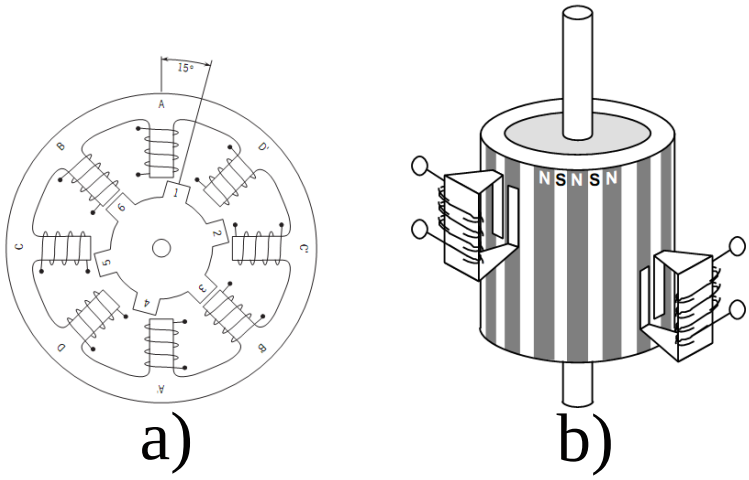

Figure 2.2: *a) Variable-reluctance (VR): This type of motor consists of a soft iron multi-toothed rotor and a wound stator. When the stator windings are energized with DC current the poles become magnetized. Rotation occurs when the rotor teeth are attracted to the energized stator poles. b) Permanent-magnet (PM): Often referred to as as "tin can" or "canstock" motor has permanent magnets added to the motor structure. The rotor is permanently magnetized with stripes of alternating north - south poles which are attracted to the stator when energized by the input current pulses. This is the kind of stepper motor we have implemented in this work.*

Finally the driving of a stepper motor can be classified in two major groups: Unipolar and Bipolar driving. A bipolar motor with two phases has one winding around the stator. On the other hand a unipolar motor with two phases has one winding but with

[1]Figure 2.2 is adapted from an Ericsson industrial circuits application note: *"Stepper Motor Basics"*.

a center tap per phase (see fig. 2.3)[2]. This last type of motor driving (unipolar) is the one that has been implemented in this work.

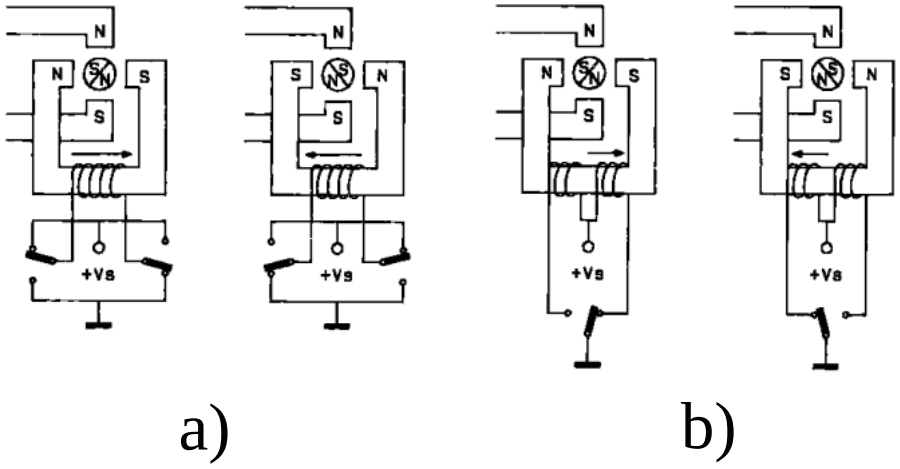

Figure 2.3: *a) Bipolar Driving: This type of driving requires the current in the same stator winding to be reversed. Electronic control circuits involving H-bridges are required to perform this task. b) Unipolar driving: This type of driving also has one winding around the stator but with a center tap or connection to a source voltage (VS). No current reversal is needed in this type of driving, just the correct input sequence is required.*

2.1.2 Electronic Control Circuit

The circuit designed for the unipolar driving of our PM Stepper motor is shown in the following schematic (see fig. 2.4). The central part of this circuit is the integrated microcontroller PIC16F684 [15] which is programmed to execute the input logic required by the stepper motor using unipolar driving [3]. This microcontroller chip is programmed so that the frequency and direction of the input sequence is controlled

[2]Fig. 2.3 is adapted from an SGS-Thomson microelectronics application note:*"Stepper Motor Driving"*

[3]asmStepper 4.asm©: This program was written in assembler language by Myke Predko for the MPLAB Integrated Development Environment (IDE) library by Microchip.

with a potentiometer connected to pin 3 (RA3) of the microcontroller. The logic voltage used by the PIC is 5V. This microcontroller is programmed to turn clockwise if RA3 receives more the 2.5 V and in the opposite direction if less is given as an input. If the potentiometer is at any of its extremes (0 V or 5 V), the stepper will move at its full speed. Furthermore, the angular velocity of the stepper motors will gradually slow down as the voltage received by RA3 approaches 2.5 V using the potentiometer.

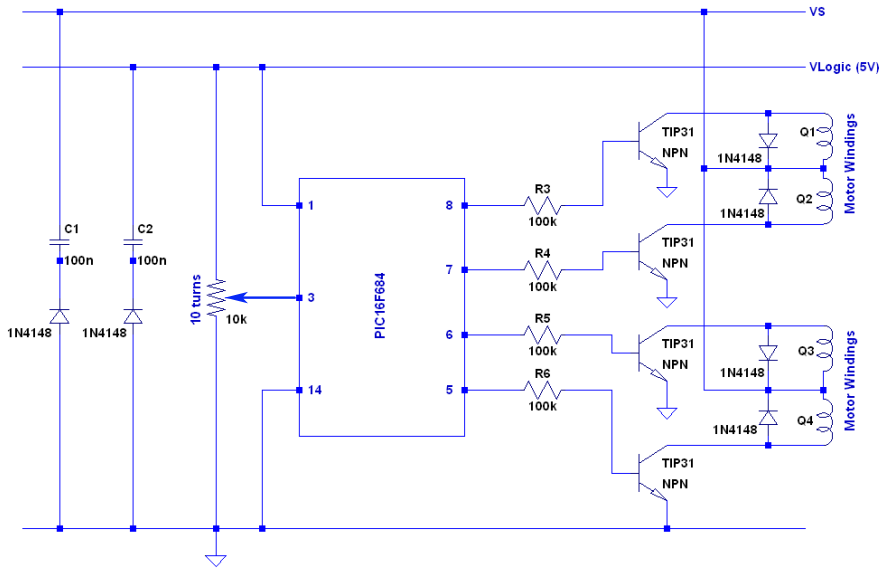

Figure 2.4: *Schematic drawing of the circuit designed for Unipolar driving. PIC16F684 belongs to the flash memory family, this means it can be reprogrammed several times. The chip is programmed on the PICkit 2 TM development programmer/debugger. In-circuit programming and debugging was preformed with the Microchip MPLAB Integrated Development Environment (IDE)*

The other important component of this circuit is the amplification or power stage conformed by a series of 4 TIP 31 transistors.[4] The colectors of these transistors are connected to the extremes of each motor winding. When the base of one of these transistors is pulsed by an input signal, that comes from the PIC microcontroller, a flow of current is generated from the center tap of the winding to the emitter, which is con-

[4]TIP 31 transistors are NPN silicon power transistors designed for power amplifiers and switching applications.

nected to ground. The center tap of each winding is connected to an external voltage source (V_S) which controls the power consumption of each winding and therefore its torque. The power consumption of each winding goes from 0.3 W to 1.4 W.

The windings (Q1, Q2, Q3 and Q4) (see fog. 2.4) move the PM rotor according to the sequence of pulses that the PIC microcontroller applies to the base of the corresponding transistors. A diagram of this pulse sequence and the corresponding energized winding is depicted in the following diagram (see fig. 2.5). It is important to remark that windings Q1 and Q2 share the same iron core, just as Q3 and Q4. These windings are only separated by a center tap connected to an external source (VS) to reverse the polarity the iron core

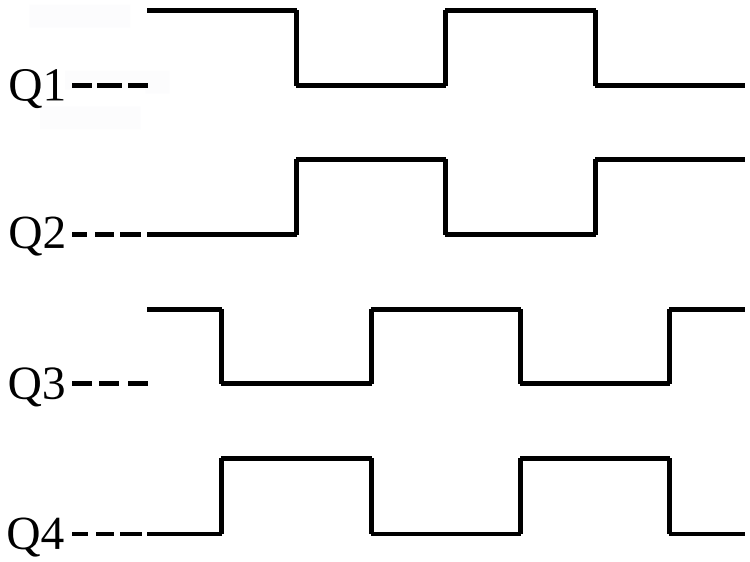

Figure 2.5: *Pulse sequence generated by the PIC microcontroller to switch on the transitors in the power stage that lead to the power consumption of windings Q1, Q2, Q3 and Q4.*

2.2 Atomic Force Microscopy

Atomic force microscopy (AFM), also known as scanning force microscopy (SFM), is a basic technique and inevitable for all nanoscopic research. Like all other scanning probe microscopes (SPM), AFM works by scanning the sample surface with a sharp tip, or more generally a probe. It operates by measuring attractive or repulsive forces between the tip and the sample in constant height or constant force mode[17]. The tip-sample force is obtained by measuring the deflection of the cantilever. The AFM is a versatile instrument that was first thought for measuring topographies of insulating surfaces which could not be measured with Scanning tunnelling microscopy (STM). The first AFM was developed in 1986[18] and the cantilever deflection was measured with a STM tip placed near an AFM conducting cantilever. Nowadays, the deflection of cantilevers is typically measured by focusing a laser beam on it and detecting variations in the reflected laser spot (see fig.2.6 a)).

The two operating regimes in which an AFM can work is associated with the type of tip-surface force that is measured. In the repulsive regime the AFM operates in the so called contact mode while in the attractive regime it is said to operate in the non-contact mode (see fig. 2.6 b)).

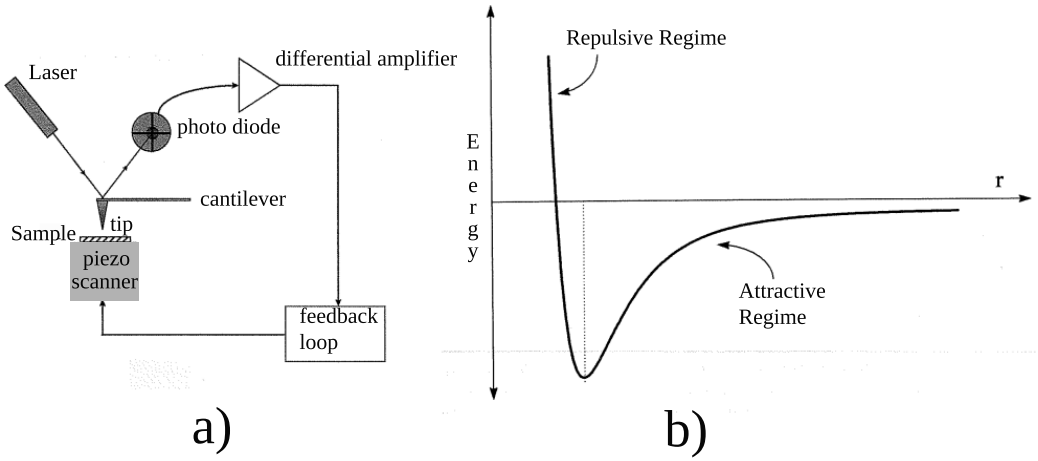

Figure 2.6: *a) Typical AFM experimental setup. b) Lennard-Jones Potential that is used to model the Tip-Surface interaction energy. Contact mode operates in the respulsive regime and non-contact mode operates is the attractive regime. Both images have been adapted from [19]*

In the contact mode the tip measures the repulsive forces between the tip and the sample surface. The tip is dragged over the surface while the magnitude of the interaction force (measured with the reflected laser spot) is kept constant with a feedback loop, creating a surface image of the sample. On the other hand the in non-contact mode, the tip-surface force is obtained by vibrating the cantilever near its resonance frequency and measuring variations in the amplitude of its oscillation as it scans a surface. Changes in the amplitude of the cantilever's vibration are related to tip-surface interaction forces and therefore distance to the surface. The surface topography is obtained by keeping this amplitude constant with a feedback loop.

For soft films like the ones studied in this research have used an operation mode called **intermittent contact mode or tapping mode**. This technique operates intermittently in the contact regime. It consists of vibrating the cantilever near the resonance frequency and measuring the amplitude and phase of the laser spot with a phase sensitive amplifier. The feedback loop maintains the amplitude of the measured vibrating laser spot constant to generate the surface topography, like in the non-contact mode. The only difference is that the tip enters the repulsive regime every time it taps the

surface.

Intermittent contact mode effectively reduces lateral forces given that the tip spends less time on the surface. This is useful to us because it means that delicate samples such as molecular films can be imaged without severe damage of the sample. Another characteristic that makes this mode an optimum technique for studying n-alkane thin films is that it avoids capillary forces which appear due to thin water films that form on the surface of the sample. This thin water film forms naturally due to the ambient conditions in which our AFM operates.

2.3 Scanning Electron Microscopy and Energy Dispersive Spectroscopy

Scanning Electron Microscopy (SEM) is also a SPM technique just as AFM, although SEM was developed much more earlier. The probe used in SEM to scan a surface is a beam of electrons that is emitted from an electron gun that in our case consists of a thermoionic tungsten emitter. The electron are then accelerated by a bias potential, ranging from 50 kV to 0.2 kV, and latter focused onto the sample by a series of electron lenses. These electrons are often referred to as the primary electrons (PE) and are focused on a spot that is a few nanometers wide. This spot scans the sample by deflecting the beam with a series of coils (see fig 2.7 a)). As this electron probe scans the sample, electrons and X-ray radiation is emitted from it. The emitted electrons can be classified in two groups: Secondary Electrons (SE) and Backscattered Electrons (BSE) (see fig. 2.7.b) **upper image**). SE are energetically lower than the BSE. The SE are generated by multiple inelastic scattering of the electron with the atoms of the sample. On the other hand BSE are generated by inelastic (that includes Auger electrons AE) and elastic scattering (see fig. 2.7 b) **lower image**). The type of electrons we measure in this work are collected with the SE detector, usually a Everhart-Thornley detector[20]. The intensities collected with this detector are then projected on a screen with a Cathod Ray Tube (CRT) that is synchronized with the scanning coils to obtain a surface image.

The other technique that we have used to analyze our films is **Energy Dispersive**

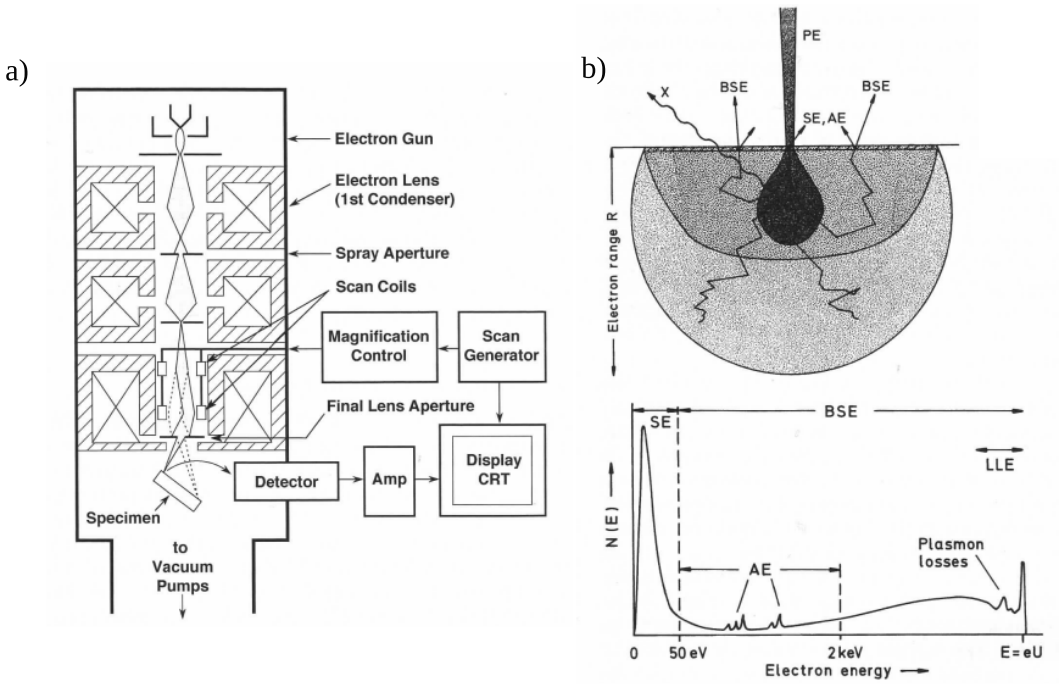

Figure 2.7: *a) Simplified view of a SEM. (image from [20]) b)* ***Upper image****: The pimary electron beam (PE) generates diverse processes that liberate Secondary electrons (SE) Backscattered Electrons (BSE), Auger Electrons (AE) and X-ray radiation (X).* ***Lower image****: Number count versus energy of the different types of electrons liberated by the focused electron probe.(images from [21])*

Spectroscopy. This technique consists in the collection of X-ray radiation generated by inelastic collisions of the PE beam. The detection of X-ray radiation is carried out with a semiconductor element. This element is usually a p-n junction of Si(Li) that is reverse biased to obtain an intrinsic depletion zone where the x-rays generate electron-hole pairs [21]. These electron-hole pairs are than counted as electric pulses and the energy of these pulses can be related directly to the energy of the incident X-ray. Chemical information of the film composition can be obtained using the collected x-ray spectra, given that every element has its own characteristic x-ray peak.

Chapter 3

Results and Analysis

In this chapter we shall present the results obtained by the dip-coating technique. The first samples presented here are samples 10050 and 10070 that are manually withdrawn from the solution, in such a way that the solvent evaporates as the sample is pulled (see fig. 1.5 a)). These two samples are studied with AFM. The solutions that samples 10050 and 10070 are dipped in are made of 10 mg and 17 mg of C32 disolved in 20ml of C7, respectively.

The other samples presented in this chapter are labelled as the **ST** family and are studied using SEM and EDS. There are a total number of 22 ST samples prepared, each with its own solution. All of these samples are prepared with our velocity controlled dip-coating setup, covering withdrawal velocities from 0.2 cm/min to 6 cm/min in discrete steps of $\sim 10\mu$m. ST samples are dipped in solutions of 15mg of C32 disolved in 20 ml of C7.

3.1 Sample 10050

This sample is manually withdrawn from a solution of 10mg of C32 disolved in 10 ml of C7. The C32 molecules are disolved within the Heptane solution using a 15 minute long sonic bath. The silicon wafer is first cleaned following the procedure described in chapter 1. After cleaning, the silicon substrate is submerged in the solution without letting the tweezers touch the air/solution interface in order to maintain the solution

as pure as possible and obtain an unperturbed contact line at the interface. This way part of the substrate is left without coating. This sample is then withdrawn manually at a slow velocity in order to let the solution evaporate as the sample is dragged out of it. The time it takes to pull the substrate out of the solution is roughly a minute.

After the dip-coating process the sample is analyzed with AFM. A total of 3 different (30 x 30) μm^2 zones, separated by hundreds of microns, are scanned. The AFM is operated in intermittent contact mode (described in chapter 2). The cantilever resonance is found at 304 khz, but is set to vibrate at a slightly shifted frequency (303khz). A representative image of one of the 3 zones is shown next with a respective line section (see fig. 3.1). This image corresponds specifically to zone 3

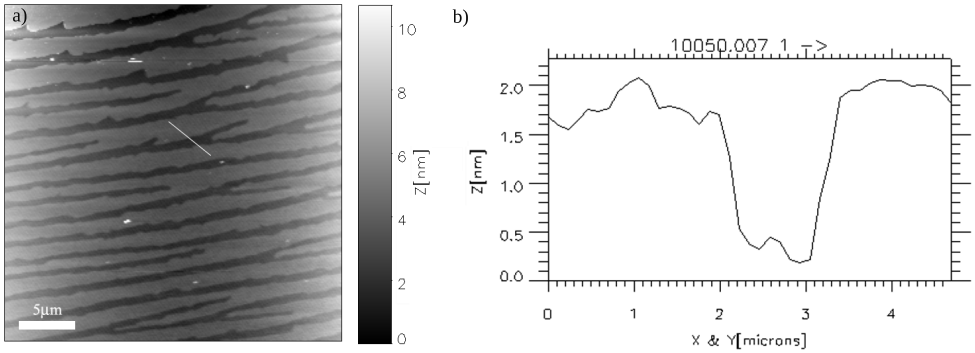

Figure 3.1: *a)Top-view of (30 x 30) μm^2 of the sample. b) Line section of the sample; this line is cut where the white line is shown in the top-view image*

A total number of 80 steps are analyzed for the three different zones. Table 3.1 summarizes the averaged step height, width and periodicity of the stripe like structures found.

Zone	Number of steps measured	Height nm	Width μm	Periodicity μm
1	22	2.79 ± 0.27	1.97 ± 0.42	1.99 ± 0.39
2	37	3.2 ± 0.45	2.28 ± 0.43	2.30 ± 0.42
3	21	1.85 ± 0.16	2.02 ± 0.34	1.98 ± 0.29

Table 3.1: *AFM line section measurements in the 3 analyzed zones.*

The average step height over the three analyzed zones is 2.73 ± 0.67 nm. We can see that zone 3 is far from the values that are found for zones 1 and 2 (see fig. 3.2). This may be caused by the use of different set-point values in the feed back loop with respect to zones 1 and 2. Assuming that a parallel bilayer covers almost completely

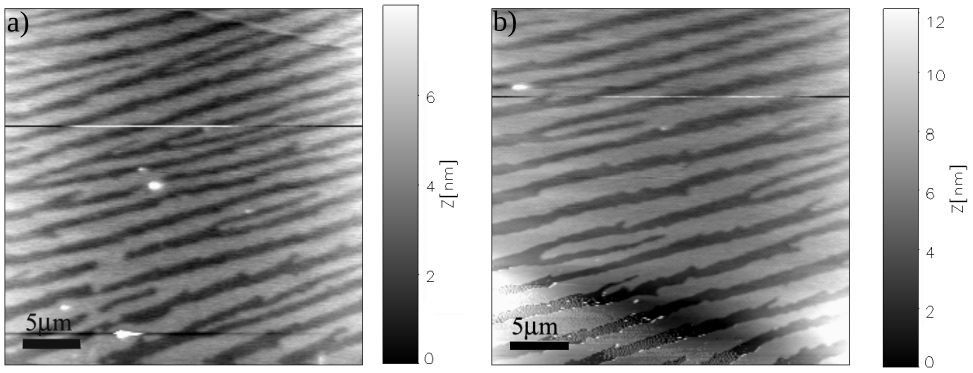

Figure 3.2: *a)Zone 1, the bulk particle seen near the center of the image was measured to be ∼ 10 nm high. b) Zone 2*

the substrate and that the AFM measures the step from this bilayer to the first perpendicular, the average value of 2.73 nm is still far from the expected all-trans value of the molecule (4.25 nm). A first explanation would be that the molecules of this first "perpendicular" layer are slightly tilted, but this contradicts recent X-ray diffraction experiments done on films with similar preparation [10], that supports the perpendicular layer model. A definitive explanation for this contradiction between AFM and X-ray measurements came from M. Bai et. al [9] who referred to this effect as a false step. This false step is explained to occur due to the different adhesion forces that the AFM tip measures when going from the parallel bilayer to a first perpendicular

layer of C32. This change in interaction forces affects the measurement of the true step height as proposed in [9]. This false step can be calibrated by using the phase channel signal and force curves measurements as proposed in [9]. This reported false step was found to shift the height up to 20% of the true value, leading to a $\sim$ 3.7 nm step height of the first perpendicular layer. Our measured value for this step (2.73 nm) is almost 1 nm below the false step reported in [9]. This difference between our false step and the reported one could be due to the different set-point values used in our measurements with respect to the reported ones in [9]. Another reason that could explain the discrepancy between the reported and measured false step could be related to a combination of physical effects such as a small tilt of the molecules or an uncomplete parallel bilayer. Force curves and phase channel measurements are required to answer correctly to these questions, as proposed in [9].

Finally, the average width and periodicity in the three measured zones is 2.20 $\pm$ 0.40[μm] and 2.13 $\pm$ 0.41 [μm] respectively. These three zones present stripe like structures of no more than one perpendicular layer and few evidence of bulk particles. As we will see further on in this chapter, these stripes grow parallel to the pulling direction.

3.2 Sample 10070

This sample is prepared using a similar procedure as sample 10050. The main difference is that a greater concentration of C32 molecules is disolved in C7. The dipping solution is made of 17mg of C32 disolved in 20ml of C7. This sample is also manually withdrawn from the solution in roughly a minute.

After preparation the film is characterized using intermittent contact AFM, with which we obtain 10 scan areas separated by hundreds of microns, each of (30 x 30) μm^2. From all the images measured, only one presents stipe-like structures (see fig. 3.3). All the other scan areas present fractal-like finger structures, bulk particles and even second layers of material with no noticeable preferred direction.

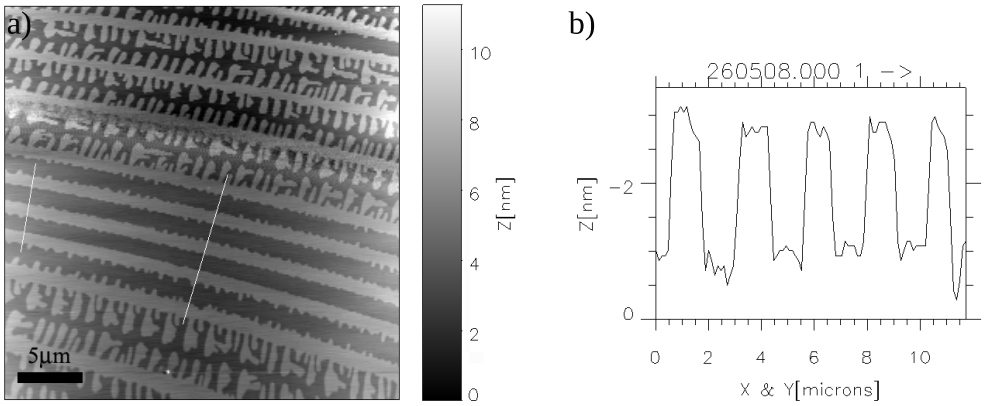

Figure 3.3: *a)Top view of the only scan area that presents stripe formation. b) Line section that belongs to the second line from left to right seen in the top view image*

A total of 8 steps are analyzed in the zone shown in fig. 3.3 a), all other zones present few signes of stripe structures. The average step height in this zone is measured to be 2.02 ± 0.12 nm. Meanwhile the width and periodicity of the measured stripes average 2.23 ± 0.27 nm and 2.33± 0.20 nm respectively.

As said before, the other measured zones did not present stripes, but fractal-like structures with no noticeable preferential direction are seen (see fig. 3.3 a)). More bulk particles and even second layers of material appear in these zones (see fig. 3.3 b)).

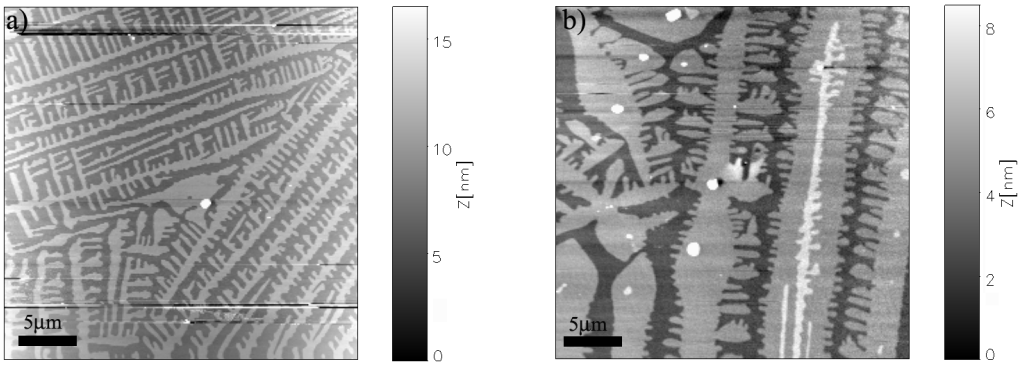

Figure 3.4: *a)Zone 2 b) Zone 9, this zone presents some bulks particles and a second layer of perpendicular molecules*

A total of 83 step heights were analyzed from the 10 measured zones. The average step height obtained for the first perpendicular layer is 2.83 ± 0.7 nm. In addition 8 step heights of the second perpendicular layer are measured from fig. 3.3 b), giving an average of 3.08 ± 0.44 nm. Finally several line sections of the bulk particles are measured in the different zones and give heights that range from 40 and 60 nm.

This sample also presents a great difference with respect to the reported false step for the first perpendicular layer, ∼ 3.75 nm. Although many zones gave averages above 3 nm, zone 1 (fig. 3.2) lowers the average and increments the uncertainty of the measurement. A rigorous calibration, such as the suggested in [9], of the step height is needed to answer the question of wether the molecules of the first layer are tilted or not. The second perpendicular layer also presents a deviation from the expected value of 4.25 nm.

The main focus of this work is not to find if these layers of molecules are perpendicular to the substrate or not, but to find how these layers depend on the withdrawal velocity. Furthermore, if there is a complete parallel bilayer adjacent to the substrate or not, is neither of great importance to this work due to the difficulty of measuring these layers with AFM and SEM. The valuable information the we rescue from these first samples is that films with an incomplete perpendicular, or nearly perpendicular layer, are grown with almost no bulk particles nor second layers of material when the substrate is slowly withdrawn from a solution with the right concentration of C32 disolved.

Other interesting facts found in samples 10050 and 10070 is the increase of bulk particles when using 17mg of C32 instead of 10mg and that fewer stripe-like structures are found when 17mg are used. A second layer is found in sample 10070 which is a key difference compared to sample 10050. The growth direction of these stripe and fractal like structures is, up to here, an open question. In fact these AFM images were taken without placing the sample with a fixed or preferential direction. The directionality of the structures shall be revealed using SEM measurements.

3.3 ST Samples

A total number of 22 samples are prepared with our velocity controlled dip-coating setup described in chapter 2. The analysis of these sample is done with SEM and EDS immediately after preparation. All ST samples are dipped in a solution of 15mg of C32 disolved in 20ml of C7, having each its own solution.

In this section, the samples will not be shown in a chronological order; they will be presented in such a way that a clear emphasis is made on the major differences seen when the withdrawal velocity is varied. The coverage and morphology of the generated structures will be analyzed and then the thermal stability of the samples will be discussed.

The first samples shown are samples ST008 and ST011. These first samples will give us a first insight on how the coverage and morphology depends on the withdrawal velocity, given that each one is withdrawn with two different velocities.

After the first rough insight described above, a more careful study of the withdrawal velocity dependence is presented. A series of 8 samples, in which we have varied carefully the withdrawal velocity from 0.2 cm/min to 6 cm/min, is shown. Each of these samples is pulled out at one single velocity. The coverage and morphology dependence on withdrawal velocity is later be discussed.

Finally, samples ST005 (U = 0.2 cm/min), ST004 (U = 1 cm/min) and PM001 (U = 1 cm/min), that are also withdrawn with a single constant velocity, shall be presented to analyze the thermal stability of the submonolayer structures.

3.3.1 Samples ST008 and ST011

These two samples are dipped in different days and solutions in such a way that the tweezers are kept away from the air/solution interface in order to obtain an unperturbed C7 contact line. This means, that after dipping there should be an interface that separates zones with and without material deposited on the silicon. We will call this interface the *contact line region*. We shall be able to directly see this region in our SEM images.

The withdrawal velocity, controlled by the stepper motor, is set at 1 cm/min. Before turning the motor on, a full manual turn of the micrometer screw is done within roughly a second. This full manual turn is equivalent to 500μm in the pulling direction, which means that the sample is withdrawn at $\sim$ 3 cm/min before turning the stepper motor on. Immediately after this rapid manual turn, the stepper motor is activated to start withdrawing the samples at 1 cm/min. This way we have two withdrawing velocities on one same sample: $\sim$ 3 cm/min and 1 cm/min. This procedure will give us a first rough insight on the films withdrawal velocity dependence.

After preparation these two samples are characterized with SEM. The SEM is operated in high vacuum conditions and a secondary electron detector is used to form the images. The primary electron beam is accelerated to the substrate by a 25kV bias voltage.

The first sample shown is ST008, see fig.3.5 and fig. 3.6. To analyze the directionality of the formed structures we search for the contact line region. This region can be seen in fig. 3.5, which is a scan area of (2.5 x 1.8) mm^2 at a 100 times magnification[1]. In this image we can clearly differentiate between a zone with material (light grey color) and another without (dark grey color). Therefore we can identify that the pulling direction of the sample is perpendicular to the interface at the contact line region.

[1]From now on we will use the notation: *100x magnification*

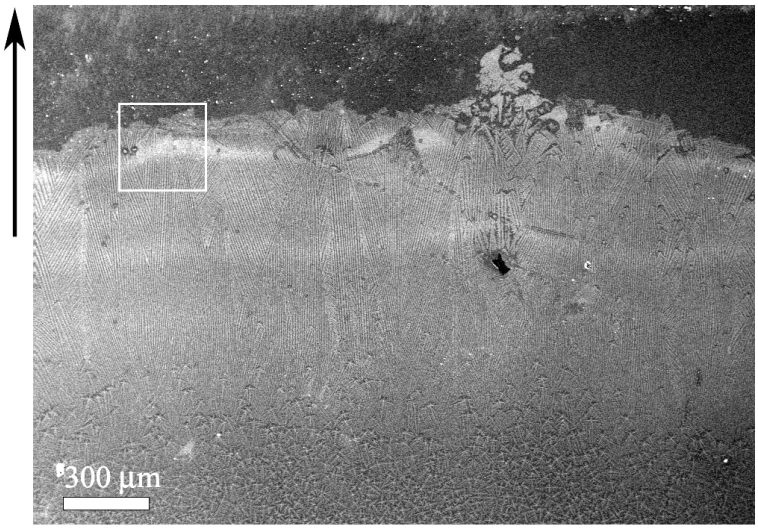

Figure 3.5: *a)We can clearly identify an interface generated by the partial dipping of the substrate. The light grey zone represents the zone that was initially submerged in the solution while the dark grey zone corresponds to the bare silicon substrate. We can see that the film is not uniform; this will be shown in fig.3.6. The arrow on the top left indicates the withdrawing, or pulling, direction. The square on the top left indicates where a series of magnification images, shown in 3.6, start.*

After obtaining this image we focus our scan area to the white square on the top left side of figure 3.5. In figure 3.6 we show a series of 6 images of 300x300μm at 500x magnification that are obtained by moving this white square in figure 3.5 in the opposite direction to the pulling direction. As we can see, figure 3.6 a) corresponds to a magnified image of the white square in figure 3.5, the other images corresponds to different areas obtained by moving this white square down figure 3.5. The black scale bar on the bottom left side of each image in figure 3.6 corresponds to 50μm.

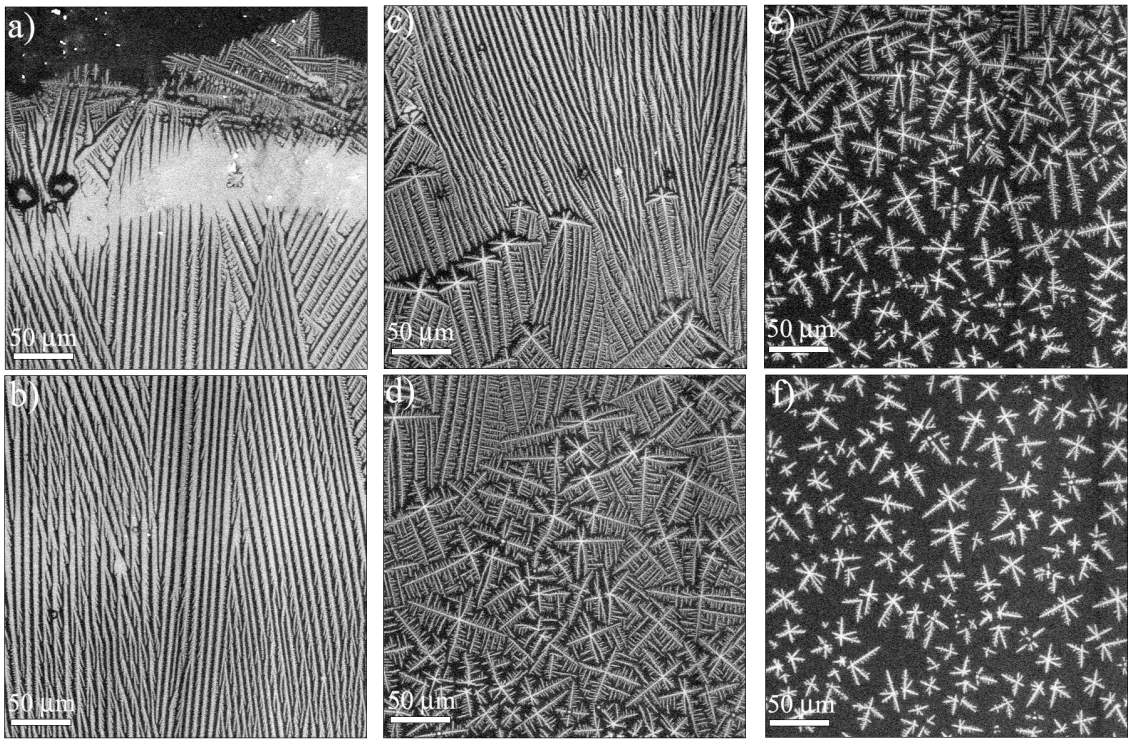

Figure 3.6: *a) Interface generated by the partial dipping of the substrate, we can see that stripe structures are formed below this interface. b) Stripe structures are found in this image c) Large dragon fly structures start to form and tend to stretch in opposite direction to the pulling. Stripe structures are still predominant. d) Dragon fly structures start dominating in this image, although they are smaller than the ones found in the last image. e) These dragon fly structures get smaller and more spaced f)* Finally we can see small dragon fly structures with a lower first perpendicular layer coverage than in the first images.

We can better visualize figure 3.6 by thinking of it as a same image where one square is placed on top of the other leaving figure 3.6.a) on top of the stack. From this image it is clear that the morphology and the coverage of the film varies along the pulling direction. This means there is a difference due to the two different withdrawal velocities used to prepare the sample. We can see that stripes are formed in the region where the sample is pulled out at $\sim$ 3 cm/min and that these structures gradually transform into dragon fly structures, as the observed also in [10]. We believe that the

precursor C7 film stabilizes at 1 cm/min in the zone where dragon fly structures predominate (see fig. 3.6 f)). The stripes seen (see fig. 3.6 a)) are oriented parallel to the pulling direction. Dragon fly structures also have a certain directionality, stretching in a direction opposite to the pulling (see figs. 3.6 c), d), e), f)).

Sample ST011 is prepared in the same way as ST008 and very similar results are obtained. Stripes of material form near the contact line region and are parallel to the pulling direction. The contact line region is shown in the scan area of 2x1.3mm^2, taken at a magnification of 100x (see fig. 3.7).

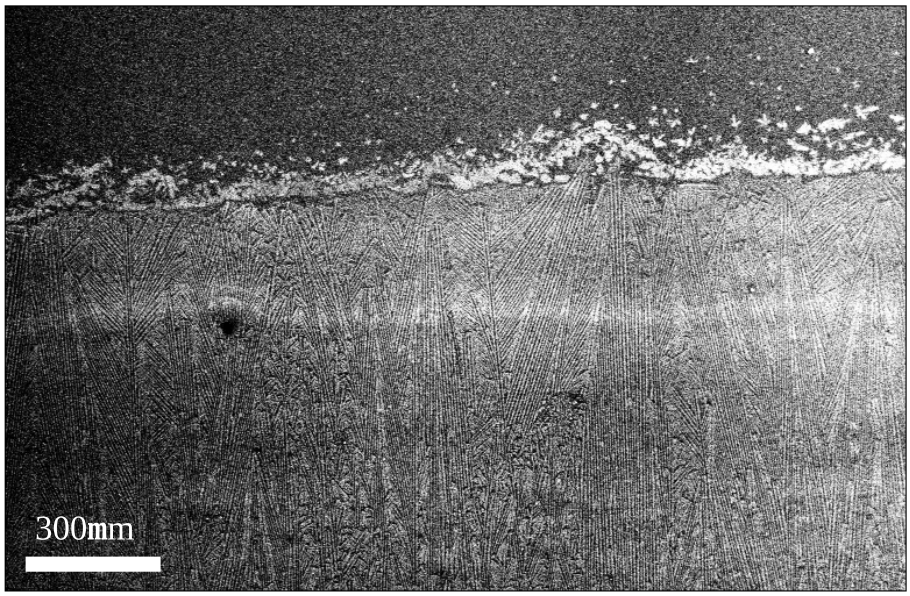

Figure 3.7: *The stripes seem to enter further into the sample and appear to be more regular.*

Magnified images of the stripe region are taken at 500x and 2000x magnification (see fig. 3.8). The stripes appear to be more regular that the one seen in ST008. Near the center of figure 3.6 a) we see a rectangle that is slightly darker, this corresponds to the zone where the 2000x magnification is taken (see fig. 3.6 b)). We can see from these images that concentrating our electron beam to smaller areas damages the film.

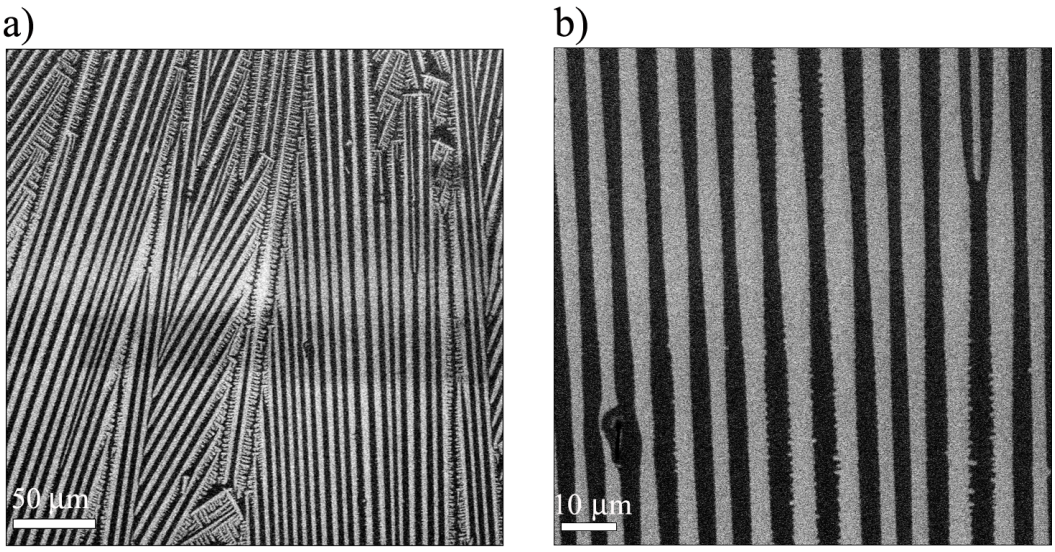

Figure 3.8: *a) (300 x 300) μm^2 scan area at 500x magnification. b) (90 x 90) μm^2 scan area at 2000x magnification.*

After this stripe region, dragon fly structures start appearing gradually as we move down the sample in opposite direction to the pulling (see fig. 3.9). Three images at 500x, with scan areas of (300 x 300) μm^2 show this gradual change from stripes to dragon fly structures in sample ST011.

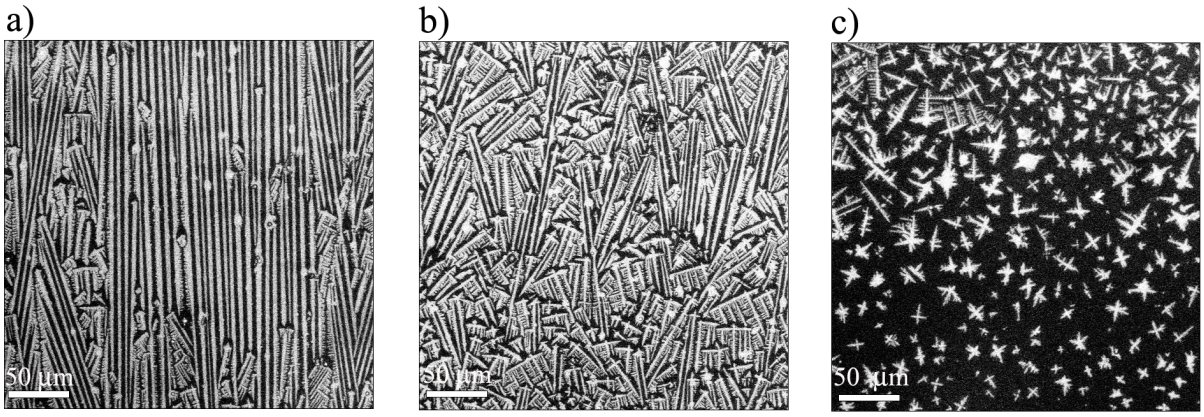

Figure 3.9: *a)Large dragon flies start appearing. These stretch in the direction opposite to the pulling. b) These stripes are smaller. c) Final size of the dragon fly structures, the coverage is clearly lower than in the first image.*

We can see that ST008 and ST011 behave in similar ways, presenting two types of structures that appear due to the different withdrawing velocities that are used on each sample. This tells us that the morphology and coverage of the structures is determined by the withdrawal velocity. The structures in these two samples gradually change from stripes to dragon flies as the air/solution interface moves across the sample, which means that the change in velocity does not instantly affect the structures. There is a certain transition zone from stripes to clear dragon fly structures.

The stripe structures that we find in these two samples are larger than the ones found in 10050. The width and periodicity of these stripes are $\sim 8\mu$m, and 4 μm respectively, which is nearly four times larger than the values found in 10050. This difference could be related to the withdrawal velocity. The generated stripes dependence on the concentration and withdrawal velocity is beyond the scope of this work. We will center our attention over the next sections on the coverage and morphology of the first perpendicular layer as a function of withdrawal velocity and will find the conditions that lead to stripe structures.

3.3.2 Sample ST006

This sample is dipped partially in the C32 solution. ST006 is withdrawn with a single constant velocity of 1 cm/min. This withdrawal velocity was repeated for 2 other samples (ST004, PM001) and give very similar results to sample ST006. The other samples, that were prepared at 1 cm/min, will be shown later as part of the thermal stability discussion.

After dipping ST006, several SEM images are scanned at 25 kV acceleration bias; in addition, EDS analysis at different beam energies is performed on the dragon fly structures that are found. The following images show two 2 x 1.3 mm^2 scanned areas of the contact line region and near the center of the sample at 100x magnification (see fig. 3.10). The white scale bar at the bottom left of figure 3.10 a) and b) indicate 300μm. We can see a minimum presence of bulk particles and a very homogenous dragon fly coverage.

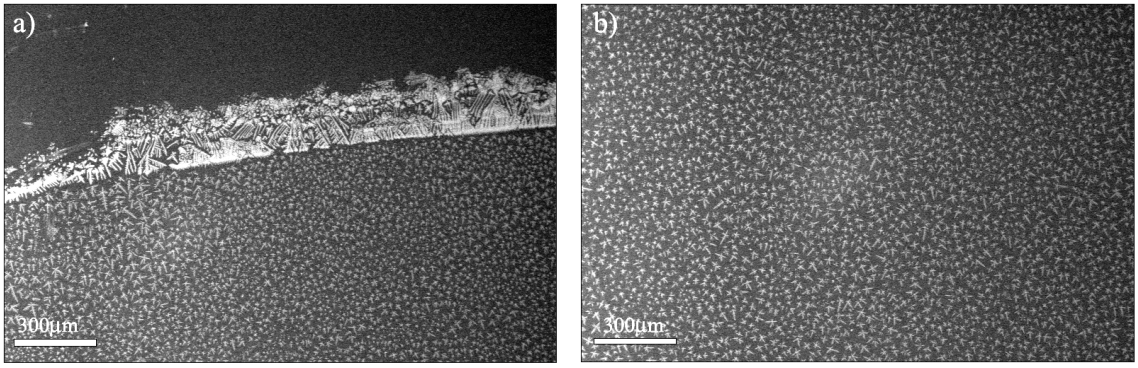

Figure 3.10: *a) Contact line region. b)Near the center of the sample, almost no bulk particles can be seen.*

Two (300 x 300) μm^2 scan areas are shown in figure 3.11 a) and b). These images are taken at 500x in zones that are separated by several millimeters. The white scale bar indicate 50 μm

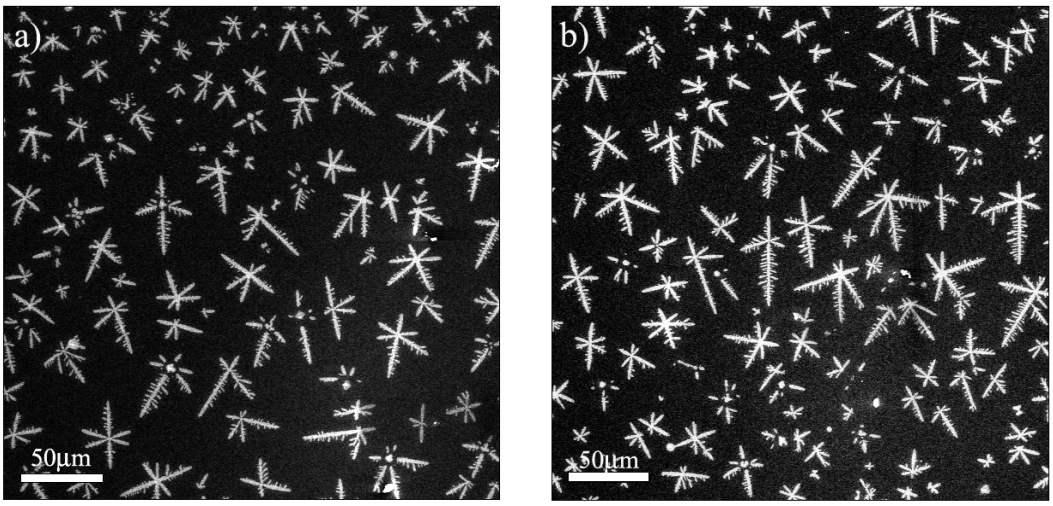

Figure 3.11: *Two magnified areas showing dragon fly structures*

A series of 8 images such as the shown in fig. 3.11 are obtained to calculate the coverage of the first perpendicular layer seen in white color. These images are first changed from grey scale to black and white images. Then dividing the number of white pixels by the total number of pixels we obtain the percent coverage of the first perpendicular layer. The coverage, measured on 8 images like the shown in fig. 3.11, gives an average of 10.75 $\pm$ 0.31 %. More coverage measurements are done for other samples prepared at different withdrawal velocities. These measurements shall be shown in the next sections.

Other interesting features to measure in these samples are the isotropy of the dragon fly structures and the length of the finger instabilities that grow on these structures (see fig. 3.12). In figure 3.12 we will explain how we measure the isotropy and the instability length of the generated structures.

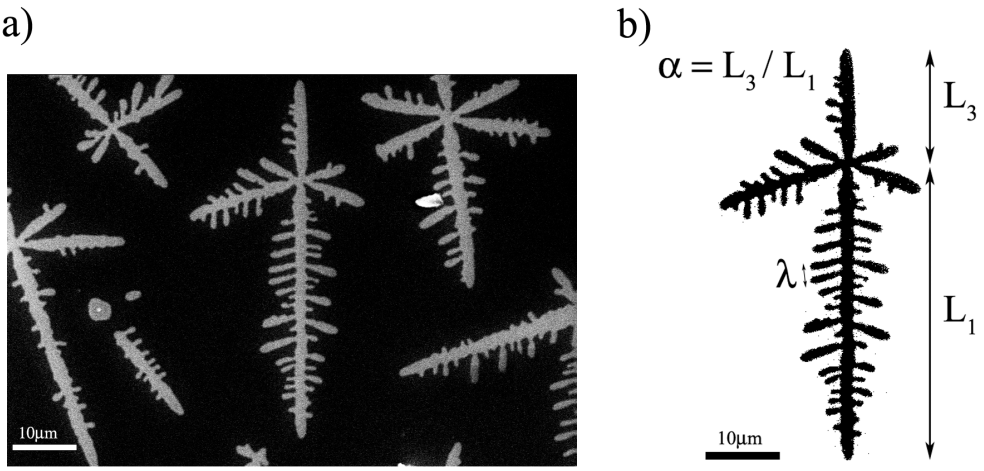

Figure 3.12: *a) Scan image of (88 x 60) μm^2 at 4000x magnification. A clear dragon fly structure appears in the middle. b) We define the isotropy parameter of these structures as the ratio between the fingers that point in the withdrawal direction (L_3) and the larger finger the points against the withdrawal (L_1). The instability length λ shall be defined as the distance between the nearest sub-fingers that appear from one of the main fingers as seen in this image.*

In figure 3.12 b) the main fingers measure L_3=15.75μm and L_1=39.19μm, giving an isotropy of α=0.4. A perfectly isotropic dragon fly, like a see-weed figure, would give a parameter α=1; on the other hand, when L_3 is very large, like in stripe structures, α would tend to zero. A total of 25 isotropy measurements are done for this sample giving an average of 0.46 $\pm$ 0.11 Meanwhile the length of the sub-finger instability, averaged over a number of 52 measurements, is 1.52 $\pm$ 0.28μm.

The final analysis done for this sample is EDS. This type of analysis is not repeated for other samples. We mainly wish to show these results to demonstrate that these dragon fly structures are in fact, carbon based (C32). The acceleration voltage of the

incident electron beam was lowered gradually from 25kV to 1kV (see fig. 3.13). At 2kV we are able to see a carbon peak in our spectra. For these measurements, a different dragon fly structure was chosen for each energy, focusing our scan area to its center. The count axis in figure 3.13 is shown in logarithmic scale so that each image can be presented with the same count range and compared with another.

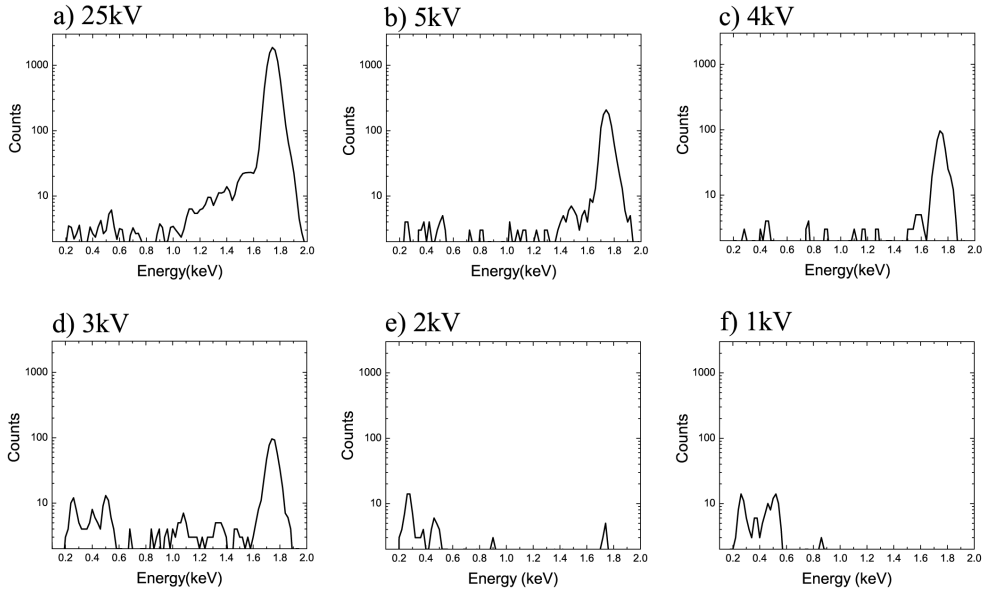

Figure 3.13: *EDS scans for different acceleration voltages with data recollection times: a)110 s, b) 300 s, c) 300 s, d) 500 s, e) 500 s and f) 500 s*

In figure 3.13 a) a clear peak centered in 1.737 keV is seen. This peak is associated to a silicon transition. In literature, this peak occurs at 1.739 keV [20] and is caused by the x-ray emission of an L shell electron filling a vacancy generated in the K shell by the PE beam. This type of transition is referred to as a Kα process. As we lower the acceleration voltage the silicon peak begins to decrease (fig. 3.13 b) and c)). In figure 3.13 a), b), and c) the chemical analysis software measures 100% concentration of silicon. This is because the PE beam is sufficiently energetic to produce transitions deep in the silicon substrate.

At 3kV (fig.3.13 d)) the silicon peak is still present, but two other peaks appear at 0.268 keV and 0.501 keV, which are related to oxygen and carbon Kα emissions pro-

cesses. The oxygen emission is reported at 0.524 keV in literature [20]. The chemical analysis was not able to estimate the concentration of carbon, but it did estimate 1.35% concentration of oxygen and 98.07% of silicon. The presence of oxygen and silicon indicates that we are at the native silicon oxide layer.

At 2kV (fig. 3.13 e)) the silicon peak almost disappears, while a clear carbon peak at 0.268 keV appears. This carbon peak in literature is found at 0.277 keV. Meanwhile the oxygen peak also is visible, but is not measured clearly by the chemical analysis software. This analysis gives a 100% concentration of carbon at this energy. This means we are mainly generating carbon transitions from the film.

Finally at 1kV (fig. 3.13 f)) the carbon peak at 0.268 keV remains and the oxygen peak at 0.501 keV grows respect to figure 3.13 e). In our chemical analysis the concentration of carbon and oxygen gives 23.34% and 76.66% respectively. These results are due to a thin layer of water that is still present on the surface of the film. This water layer can only be removed by enhancing the vacuum conditions within de SEM chamber. The silicon peak has vanished almost completely at this incident energy.

The above described procedure demonstrates that the dragon fly structures are carbon based. This is proved for the first time using EDS measurements, by gradually lowering our PE beam incident energy, confirming the results in [10].

3.3.3 Withdrawal Velocity Dependence

A group of 8 samples are prepared at withdrawal velocities varying from 0.2 cm/min to 6 cm/min, associating each sample to a single velocity. In this section we will analyze the isotropy parameter α, the instability length (λ) and the film coverage as a function of withdrawal velocity. The preparation of the film is identical to ST006, using different solutions with identical concentrations for each new sample and velocity. SEM images for these samples are taken over 4 zones separated over several millimeters at 500x and 1000x magnification with a PE beam accelerated at 25 kV bias. The coverage analysis is usually done with 500x images. Figure 3.14 shows a series of (300 x 300) μm^2 scan areas at 500x and 300x (ST005) of the samples that are withdrawn at different velocities.

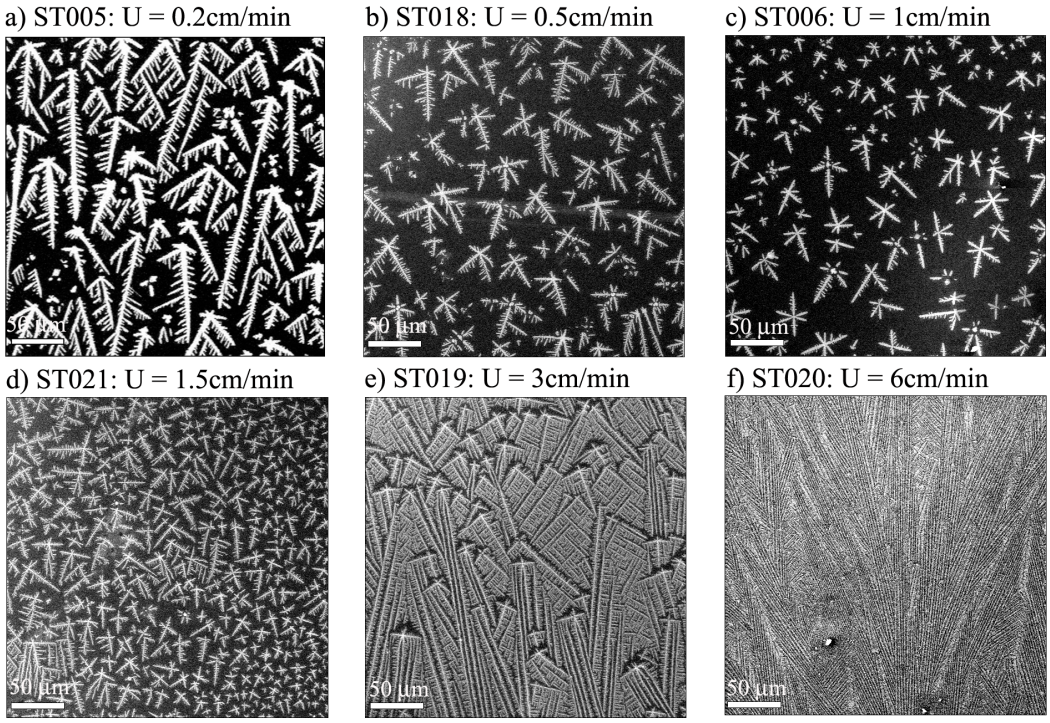

Figure 3.14: *We can see that the coverage of the film reaches a minimum near 1 cm/min. Image f) has the highest coverage and stripe structures appear here. The white scale bar marks 50µm in every image.*

As we can see from the fig 3.14, the coverage of the sample depends on the veloc-

ity. Images for velocities U=2 cm/min (ST002)and U=2.5 cm/min (ST022) are not shown in figure 3.14. Furthermore the morphology of the dragon fly varies as the withdrawal velocity changes, this can be better appreciated at 1000x magnifications (see fig. 3.15) as seen in the next (150 x 150) μm^2 scan areas.

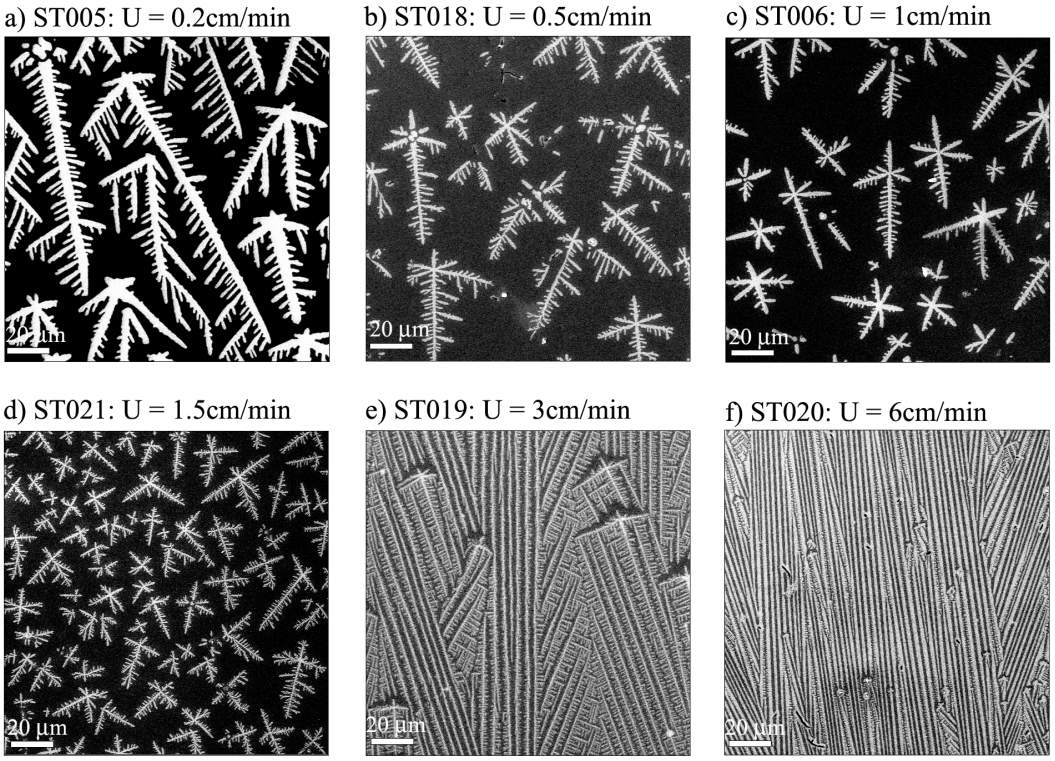

Figure 3.15: *As we can see the dragon fly structure at U=0.2 cm/min stretches against the pulling direction (L_1) but almost does not grow in the other way, (L_3). As we increment the velocity L_3 starts growing up to U = 1 cm/min. After this L_1 begins growing again until the parameter α tends to cero, at U=6 cm/min where we can appreciate stripes.*

Figure 3.15 f) shows the presence of stripe like structures. We have found evidence, that these stripes may be dragon fly structures that stretch enormously against the pulling direction. This can be seen in the next images at 3000x and 4000x.

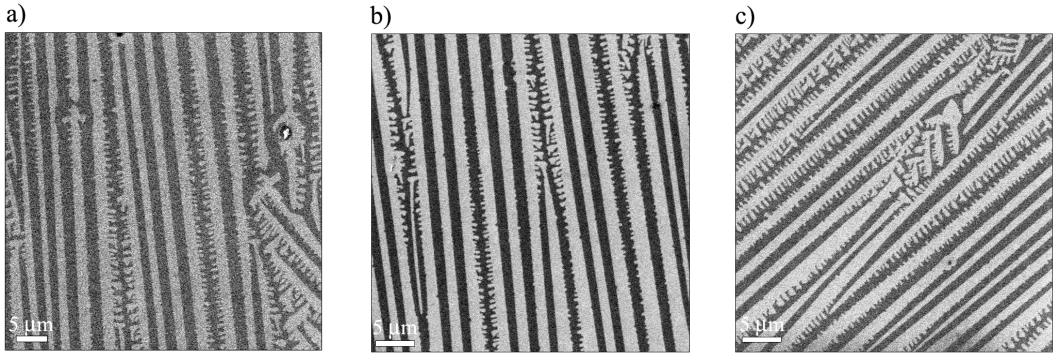

Figure 3.16: *a) (50 x 50) μm^2 scan area at 3000x. Near the top left side we can see the remains of a dragon fly structure that stretches enormously against the pulling direction. Images b)and c) are (40 x 40) μm^2 images at 4000x magnification. Stripe structures appear and finger like instabilities are seen to come out of the stripes.*

The stripes measured in sample ST020 are nearly 2μm in periodicity and 1.5μm in width, which is in accordance with samples 10050 and 10070. It is also found that these stripes are nearly six micrometers thinner and more packed together than the stripes found in sample ST008 and ST011 that were pulled out initially at ~ 3 cm/min. Although we can not pinpoint exactly at what velocity stripe structures start appearing, we do know that it is somewhere between 3 cm/min and 6 cm/min and that the withdrawal velocity affects their periodicity and width. This is as an open question and would require further study.

The first perpendicular layer coverage is measured on several images such as figure 3.14. Data recollection for coverage is performed by turning these grey scale images into black and white using the pixel histogram associated to the image. The scan areas that are taken into account are as big as they can without loosing resolution in the pixel histogram of the grey scale image. In other words, there should be two clear peaks in the grey scale pixel histogram: a light grey peak that represents C32 and a dark grey peak that represent the silicon wafer. After turning these images into black and white, these grey scale peaks narrow down to only two colors, black and white. This way, the coverage percent is calculated by dividing the number of white pixels by the total number of pixels in the new black and white pixel histogram. Given that the

amount of bulk material is minimum this procedure is adequate for our purposes.

The images analyzed have an area of (300 x 300) μm^2 and a number of approximately 10 zones were taken for each sample. We find that a scan area of (300 x 300) μm^2 is an optimum size for this analysis. Figure 3.17 shows coverage measurements of the first perpendicular layer on (300 x 300) μm^2 scan areas.

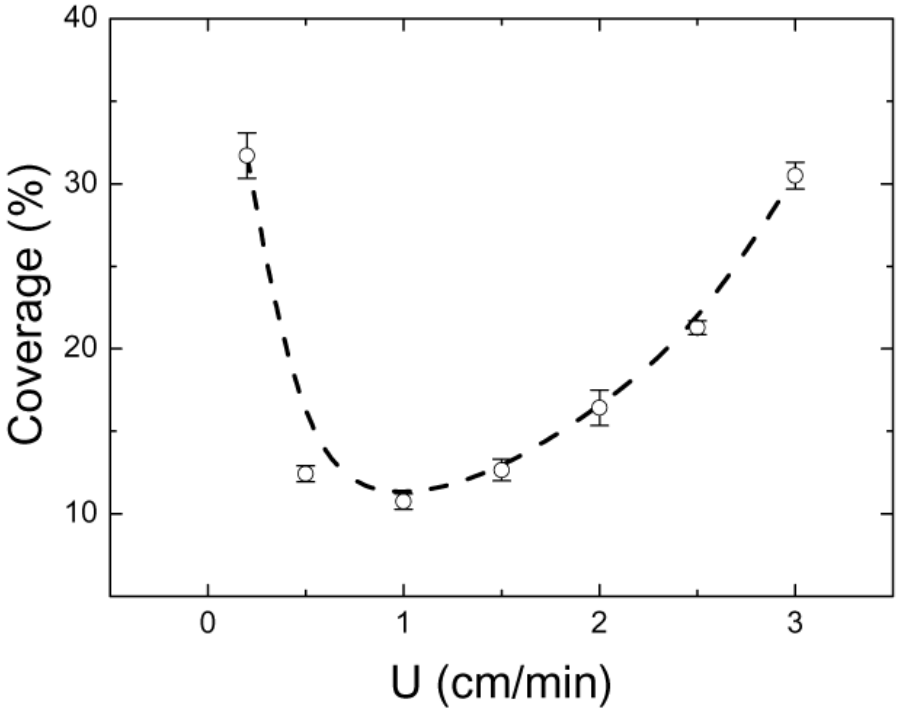

Figure 3.17: *This graph shows a range from 0.2 cm/min to 3 cm/min. The dotted line represents a parametric point connector that draws a smooth curve through the points. This point connector is called B-Spline. This type of parametric curve is continuos up to second order and does not pass necessarily through the original points, except for the first and last ones.*

For sample ST020 (U = 6 cm/min), nine scan areas of (260 x 175) μm^2 and four of (130 x 90) μm^2 were used to keep a correct peak resolution in the grey scale pixel histogram. Sample ST020 is added to the plot shown in figure 3.17 in the next image (see fig. 3.18).

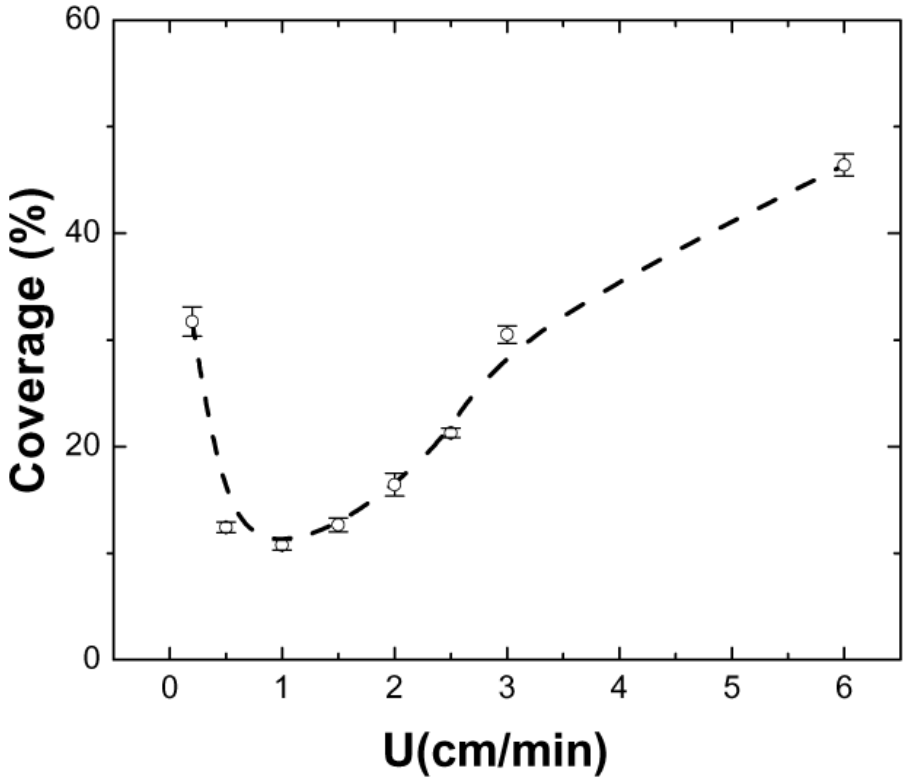

Figure 3.18: *This graph shows sample ST020. The dashed line also corresponds to a B-Spline parametric point connecting curve.*

As we can see from figures 3.17 and 3.18, the coverage abruptly falls between 0.2 cm/min and 0.5 cm/min from 30% to almost 10%. After 0.5 cm/min, the coverage reaches a minimum near 1 cm/min and starts growing steadily. In figure 3.18 we can see an inflection of the curve when sample ST020 is added, although more data points between 3 cm/min and 6 cm/min are needed to sustain this. The dotted line in both graphs are parametric curves that serve the purpose of a point connector.

Above 1 cm/min we can see that the coverage grows continuously from around 10% to almost 50% at 6 cm/min. This growth is in accordance to the entrained film regime explained in chapter 1. This idea of an entrained regime, found by M. Ghosh *et al.* in his striped films [15], is based on a work by L.D. Landau and V.G. Levich [22]. In this work the drag out of a plate from a Newtonian solution is studied and it is found that the limiting film thickness of the precursor solution film scales with the withdrawal velocity as,

$$h = 0.944 \frac{(\mu U)^{\frac{2}{3}}}{\sigma^{\frac{1}{6}} (\rho g)^{\frac{1}{2}}} \tag{3.1}$$

,where μ is the viscosity, σ is the surface tension and ρ is the fluid density. A plot of this function for a water solution, such as the reported by M. Ghosh *et al.*[15], and for a C7 solution, such as ours is shown in figure 3.19.

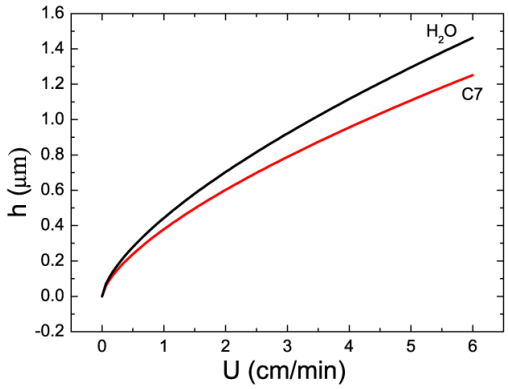

Figure 3.19: *The precursor film thickness,* ***h(U)****, for C7 in the entrained regime ranges from 0.4μm to 1.2μm*

We have not tried to fit a function such as this to our coverage measurements for U>1 cm/min because we would need more samples prepared for U>3 cm/min and are not quite sure if there is a direct relationship between **h(U)** and the coverage.

Although no fitting was attempted, the fact that our coverage grows for U>1 cm/min is of relevance. This means that there are bulk crystals disolved in C7 and they have a certain size distribution. For example, if the molecules were not clustered in bulk crystals and were all separated in the C7 solution, there would not be a coverage veloc-

ity dependence above U=1 cm/min. This is because single molecules would be able to convect to the contact line independent of the entrained C7 film thickness, and therefor withdrawal velocity. There would always be the same coverage given that single molecules are much smaller the entrained C7 film thickness for U>1 cm/min. In summary this coverage velocity dependence indicates that the C7 solution has micrometer sized bulk crystal disolved in it and that they are unstable when pinned to the silicon by the C7/air contact line, forming dragon fly structures after the pinning.

Between 0.2 cm/min and 0.5 cm/min there is an abrupt fall in coverage that could be an indication of a transition from a gravity driven C32 growth to the entrained film regime proposed by M. Ghosh *et al.* [15]. The transition from gravity driven stripe growth to entrained film growth occurs at ~ 0.01 cm/min, although the system studied by M. Ghosh *et al.* was a colloidal suspension in water. Samples at U<0.2 cm/min are required to see if this abrupt fall between 0.2 cm/min and 0.5 cm/min is actually the gravity driven to film entrained transition seen by M. Ghosh *et al.*[15].

Continuing with the analysis, the next parameter that is shown is the isotropy α vs velocity. For this parameter, around 50 dragon fly structures are measured for each sample, except for sample ST020 and ST019 which were much harder to analyze due to the large length of the structures. For these last samples the average is over 10 measurements instead of 50. The results are presented next (see fig. 3.20 and 3.21).

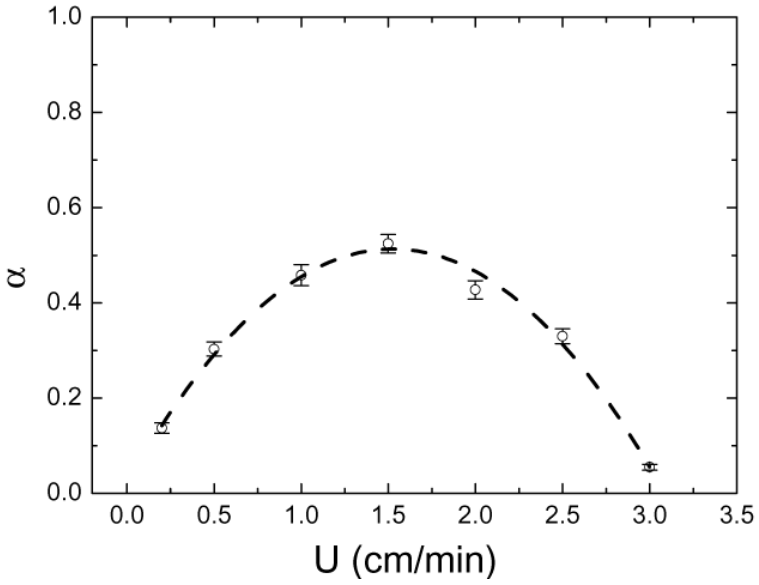

Figure 3.20: *The dashed line represents a second order polinomial fit. α=1 represent a symmetrical structure, while cero are stripe structures.*

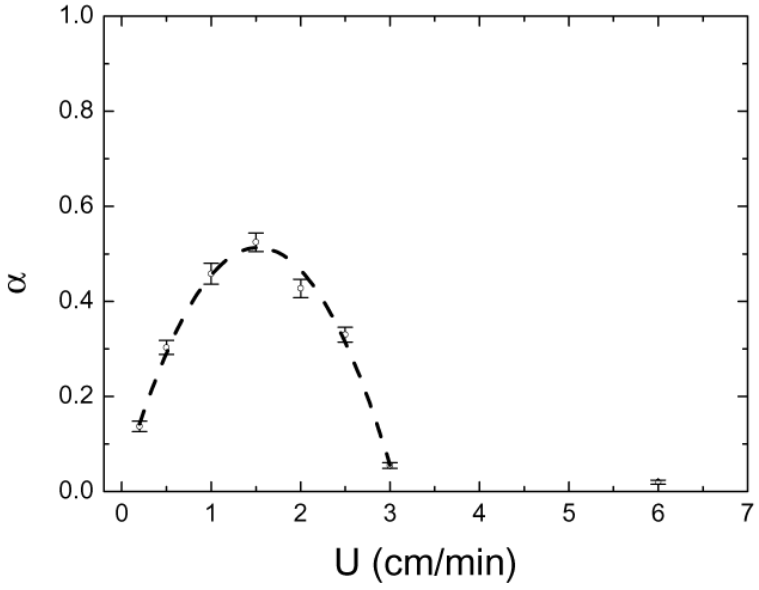

Figure 3.21: *The sample at 6 cm/min (ST020) is added to the plot and is very close to zero.*

As seen in these last graphs, α has a maximum near 1.5 cm/min and can be fitted by a second order polinomial up to U=3 cm/min. These graphs look as if the coverage vs velocity plots were turned upside down, although no clear relation between both can be seriously determined yet. We can see that before and after 1.5 cm/min the structures stretch as alpha lowers. For U=0.2 cm/min, α is near 0.15 mainly due to L_3 tending to cero. On the other hand after 1.5 cm/min the parameter starts going down due the stretching of L_1. It would be of interest to see how this parameter evolves in ranges lower to U=0.2 cm/min and between 3 cm/min and 6 cm/min.

The final parameter measured is the instability length λ. The points shown in the following plot, λ vs velocity (fig. 3.22), were averaged over 50 measurements each.

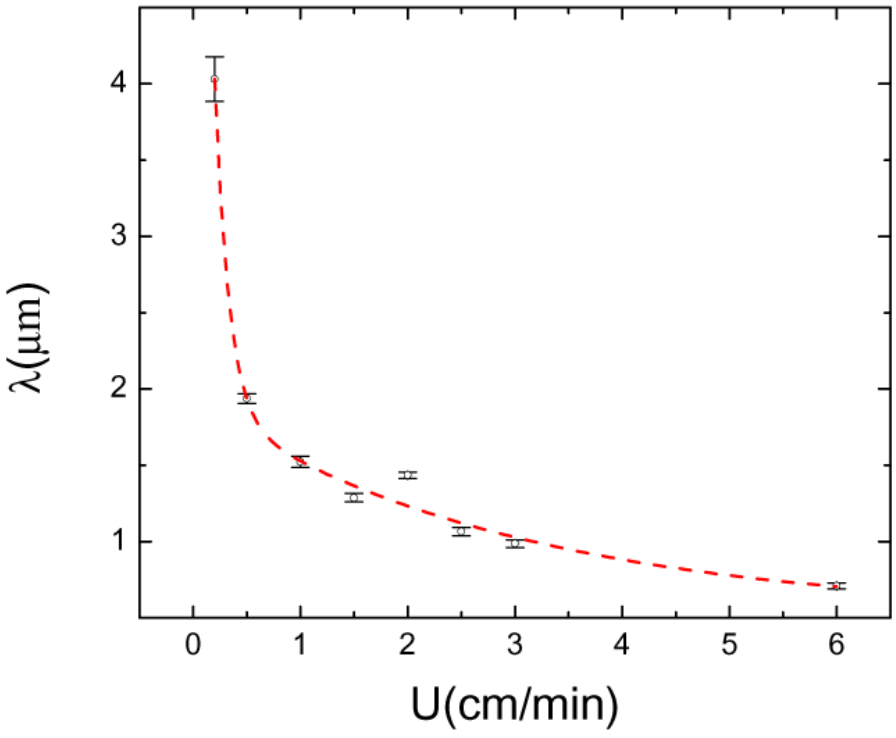

Figure 3.22: *The dashed line represents an exponential fit.*

We can see that between 0.2 cm/min and 0.5 cm/min the instability length abruptly falls from $\sim 4\mu$m to nearly 2μm. Greater changes than that are not seen at higher velocities. Given the first perpendicular layer is in fact a 2D crystal structure [10] these

measured finger lengths (λ) can be classified as a crystal growth instability [28]. The dashed line seen in the fig. 3.22 is an exponential fit of the form:

$$\lambda = A_1 e^{-U/U_{01}} + A_2 e^{-U/U_{02}} + C \tag{3.2}$$

The fact that a reasonably good fit for this plot is achieved with a sum of two exponentials is another evidence that we are in presence of two regimes, that were called by M. Ghosh *et al.*, the gravity driven and entrained film regimes [15].

All the evidences presented before indicate that the structures grown can be pinned to the silicon surface due to two different regimes. The gravity driven regimen and the entrained films regimen. Furthermore our coverage vs velocity measurements indicate that bulk crystals are mainly responsible for the C32 film growth, as the bulks convect to the contact line. Given that few bulk crystals are observed in our samples after dipping, we propose that these bulk crystals are unstable at the air/solution contact line, layering into dragon fly structures as soon as they pin to the substrate. This layering would occur due to the combined action of the C7 contact line and the interaction of the molecules of the bulk crystal with the silicon substrate (see fig. 3.23).

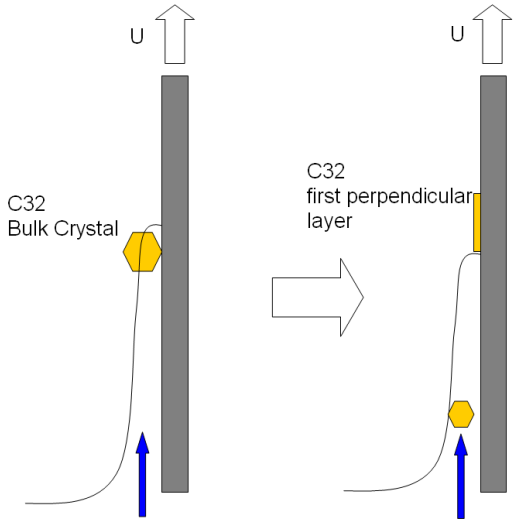

Figure 3.23: *General idea of how we believe dragon fly and stripe structures grow. The solid arrow are convection lines, that these bulk crystals follow towards the contact line.*

We propose that all the structures studied up to now are product of a combined effect of the Air/solution contact line and the silicon substrate. We can sustain this proposal because dragon fly structures are not thermally stable when they are not in the presence of the C7 contact line. This is described in the following section.

3.3.4 Thermal Stability

In this final section we shall present some results regarding the thermal stability of the dragon fly structures. As we concluded in the last section these submonolayer structures are product of the pinning of bulk C32 crystals, disolved in C7, to the silicon substrate. As the contact line retrocedes the bulk crystals start self assembling in layered layered structures (see. fig. 3.23). We believe that the coverage dependence, discussed in the last section, is an important evidence that indicates that these dragon fly structures are consequence of the combined effect of the contact line retroceding and the silicon substrate interaction with the molecules. The thermal stability of these structures is another evidence that they are product of a combined effect: contact line and silicon substrate interaction.

The first samples presented here are samples ST005 (U = 0.2 cm/min) and ST004 (U = 1 cm/min). These samples were analyzed four months after they were first prepared using SEM. Sample ST005 presents the same dragon fly structures as ST006 after the preparation. In next figure 3.24, shows scan areas of (500 x 500) μm^2 immediately after dipping (left side images) and after 4 months in ambient conditions (right side images).

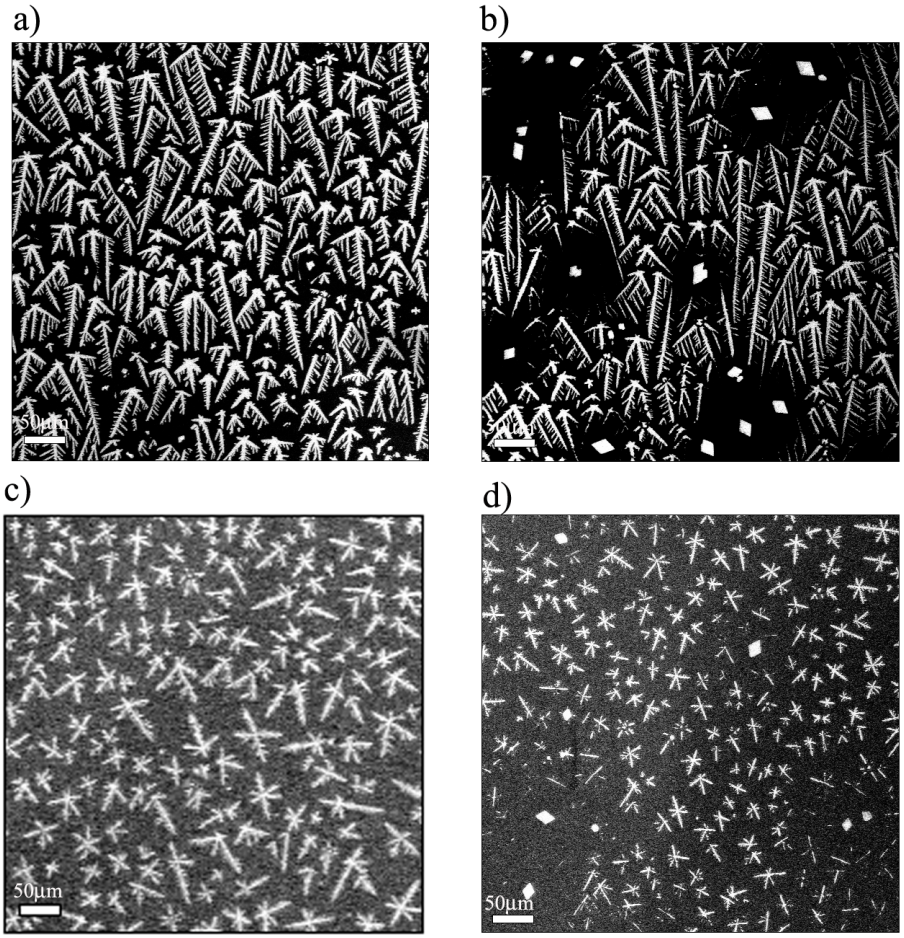

Figure 3.24: *a) 300x magnification immediately after dipping b) 300x magnification 4 months after dipping. c) 100x magnification immediately after dipping d) 300x magnification 4 months after dipping.*

As we can see, after a long period of time in ambient conditions, these structures start gathering into bulks that have a rhomboid shape. This rhomboid type shape is an indicator of the crystal structure of the bulk. These are around (10 x 10) μm^2 in lateral occupation, but we do not know how tall or how many perpendicular layers they are made of. AFM and EDS line scans would have to be performed to answer this question.

What is clear from fig. 3.24 is that these bulk crystals form a depletion zone around them. This indicates that they have gathered material from the surrounding dragon fly

structures. The main importance of this result is that even at ambient conditions (293 K) the molecules have a certain freedom to reorganize in structures more energetically stable than the dragon fly morphology found immediately after dipping. In this case the more stable structure is the rhomboid bulk crystal.

The final important thermal stability test is done by performing temperature cycles on dragon fly samples. These cycles are carried out from room temperature to 345 K and later cooled down to room temperature again. We choose 345 K because it is the melting temperature of the perpendicular layer[5]. The sample studied is pm001 (U = 1 cm/min). After one temperature cycle we appreciate a clear change in the morphology of the structures. The next image shows this sample immediately after dipping (fig. 3.25 a)) and after one temperature cycle (fig. 3.25 b)). The scan areas shown are of (300 x 300) μm^2 and are taken at 500x magnification.

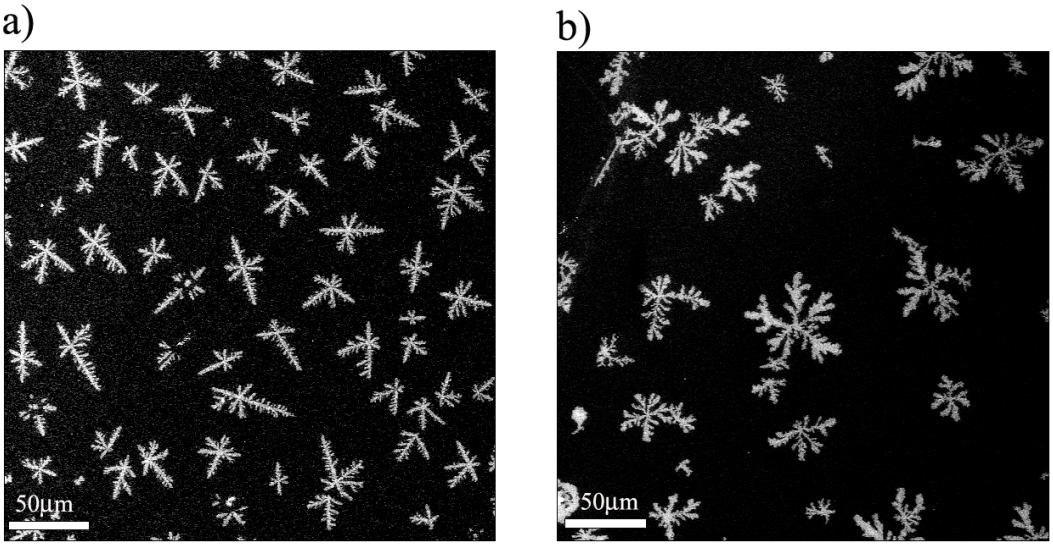

Figure 3.25: *a)Immediatley after dipping. Dragon fly structures dominate. b) After one temperature cycle up to 345K (melting temprature). Seaweed type structures dominate.*

As seen in figure 3.25 b) these seaweed like structures are comparable in size to the dragon fly structures (fig. 3.25 a)). These seaweed structures have been studied in other works using *n*-triacontane (C30) films prepared by spin coating and analyzed after several heating cycles, by A. Holzwart *et al.* [23]. It is found in [23] that these

submonolayer films also have a crystal structure with a first layer of molecules perpendicular to the substrate surface. A comparison between the submonolayer coverage films found here, before and after heating cycles, and an image from [23] showing *C30* seaweed structures is shown next (fig.3.26). The images used for the next figure are inverted and contrast enhanced to obtain black and white images where black represents the submonolayer film. The three figures shown next are (100 x 100) μm^2 scan areas.

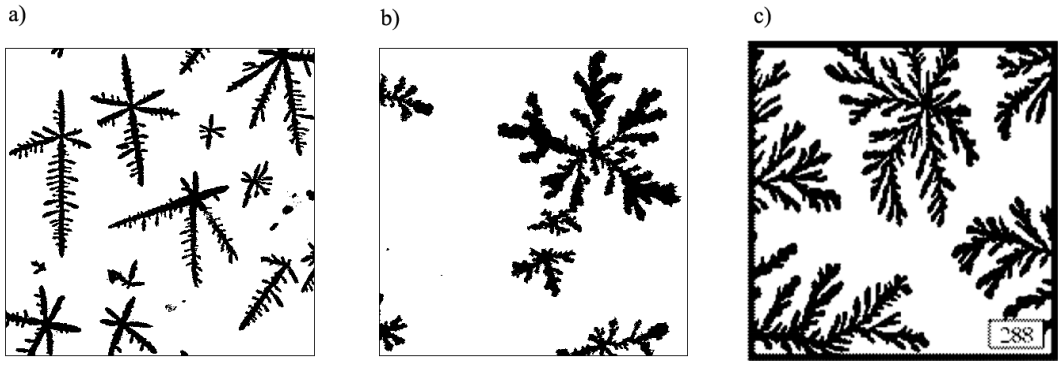

Figure 3.26: *a)Typical Dragon fly structures seen immediately after dipping. b) After a first heating cycle up to the first perpendicular melting temperature (345K), seaweed-like structures dominate the submonolayer film. c) n-triacontane (C30) submonolayer films prepared by spin coating after several heating cycles up to the bulk melting temperature for C30. This image is taken from [25]*

Image 3.26 a) and b) were taken with SEM at 1000x magnification. Image 3.26 c) was captured using an optical interference microscope. To obtain such a molecular thickness resolution, using optical methods, an artificial layer of silicon oxide, of $\sim$ 500nm, had to be grown. This molecular thickness resolution microscope was reported by R. Köhler *et al.* [24].

As we can clearly see from image 3.26 b), the seaweed submonolayer film we obtain after one temperature cycle is very similar to that from the *n*-triacontane structure obtained after several heating cycles, fig. 3.26 c), by L. Knüfing et. al[25]. This seaweed structure is very isotropic ($\alpha \sim 1$), no preferred direction for the finger growth can be noticed, unlike the dragon fly structures that have a tendency to grow larger in the opposite direction to the pulling of the substrate. Furthermore, L. Knüfing et al.[25]

studied the fractal dimension of the their obtained structures using the box counting method [26], which gave a dimension D $\sim$ 1.7. This fractal dimension is typical for growth by Diffusion Limited Aggregation (DLA) [27]. Our seeweed structure, seen in fig. 3.25 b), is also analyzed with the box counting method [2] and gives a fractal dimension of D = 1.71. With this we can affirm that our seaweed structure grows through the same mechanism as the structure found in [25] (see fig.3.26 c)). On the other hand, the fractal dimension of dragon fly structures can also be analyzed. For this purpose, we analyze sample St006 (fig. 3.12 b)) using the same box counting method as before. We obtain a fractal dimension of D = 1.56 for a typical dragon fly structure.

A final difference between the structures seen before and after heating cycles, figures 3.26 a) and 3.26 b) respectively, is that the angles formed between main fingers and between main fingers and the subfinger instabilities, are well defined. Generally in dragon fly structures we have measured angles of $\sim 30^o$ and $\sim 70^o$ between the main fingers of the structure. Meanwhile, typical angles of $\sim 70^o$ between main fingers and subfinger instabilities have been measured. Although a rigorous statistical study is required on the subject, the angles found for structures prepared at U = 1 cm/min seem to behave alike and are reproducible over the 3 samples made at this same velocity. Also, angles between main fingers of the seaweed structures (see fig. 3.25 b) have been measured giving no consequent and reproducible angle measurements between main fingers. Furthermore, the angles between the seaweed structure fingers are poorly defined, unalike the dragon fly structures.

These two differences, isotropy and undefined angles, of the seaweed structures can give us valuable information about the dragon fly structure growth mechanism. First of all, these seaweed structures grow from a melted disordered phase and start crystallizing around a central seed as the individual molecules bond to the seed (DLA). If the solution of C7+C32 in which we dip our ST samples were made of individual disordered molecules, like the C32 melt, we would expect seaweed structures instead of dragon flies to be seen immediately after dipping. This means that dragon fly structures are not formed by individual molecules pinning to the surface near the contact

[2] The fractal analysis freeware used is Fractalyse©

line. If this is not the case, then the most probable scenario is that the dragon fly structures are generated by micrometer sized bulk crystals that pin to the surface near the contact line and layer into perpendicular layers by this interface contact line. The defined angle seen in the dragon fly structures also indicates that they grow from bulk crystals similar, maybe, to the rhomboid shape crystals seen after 4 months (see fig. 3.24), layered by the retroceding contact line.

Chapter 4

Conclusions and Future Work

We have developed an experimental setup to prepare films by dip-coating at a controlled velocity. The velocity controlled dip-coating of the samples is achieved by a micrometer screw that pulls out the substrates. This micrometer screw is controlled by a stepper motor which, at the same time, is controlled by an electronic circuit. The electronic circuit controls the direction and angular velocity of the motor. A stepper motor was chosen for this setup because the torque and therefore pulling force that acts on the micrometer screw is independent of the velocity at which it turns. The torque applied on the screw is controlled by an external source and its speed is controlled by the frequency of the pulse sequence that is delivered to the windings of the motor. The achieved velocities went from 0.2 cm/min to 6 cm/min in discrete steps of $\sim 10\mu$m of the micrometer screw.

The samples prepared with velocity controlled dip-coating are silicon substrates with their native oxide layer ($\sim$15Å). The substrates are cleaned with a piranha solution and stored in extra pure water. The substrates treated with this procedure give reproducible hydrophobic clean surfaces. After cleaning, the solution in which we dip the substrate is prepared. This solution consists of n-Heptane (C7) with crystals of n-Dotriacontane (C32) disolved within using a sonic bath. After preparing this solution, the sample is dipped within it in such a way that the tweezers do not touch the solution. The withdrawal of the substrate is done slowly in such a way that the C7 evaporates as the substrate is withdrawn, leaving a film of C32 on the silicon surface.

The first samples we prepare using this technique are withdrawn manually and studied using AFM in the intermittent contact mode, these samples are 10050 and 10070. The time it took to withdraw manually these first sample is $\sim$ 1 minute. Sample 10050 was prepared with 10mg of C32 in 20ml of C7. In this sample we see stripe and finger like structures that are no more than one perpendicular layer thick. The measured step height of the first perpendicular layer for sample 10050 is 2.73 $\pm$ 0.67 nm. Almost no bulk particles are present and we do not observe more than one perpendicular layer in the three measured zones of this sample.

Sample 10070 is made with a solution of 17mg of C32 in 20ml of C7 and we observe stripes in only one of the ten scanned zones. All other zones present fractal-like finger structures with much more presence of bulk particles and even second layers of perpendicular molecules. The step height of the first perpendicular layer of this film is measured to be 2.83 $\pm$ 0.7 nm.

Although the step height of the first perpendicular layer is far from the actual all-trans length of the molecule (4.25 nm) in both samples, this error is associated to a false step height [9]. This false step is due to the interaction of the AFM tip with different adhesion forces when going from the parallel bilayer or silicon surface to the first perpendicular layer. False step heights can be corrected by AFM phase measurements and force curves performed on the different adhesion surfaces. This is left as a future work. The conclusions we come to with samples 10050 and 10070 is that submonolayer coverage films with no more than one perpendicular layer can be obtained by slowly withdrawing the sample from a solution. The solution needed for this must be made of 10 mg to 17 mg of C32 disolved in 20ml of C7. We also see that fewer bulk particles are obtained when less than 17 mg of C32 is used.

After studying these manually withdrawn samples, the velocity controlled setup is used. A total number of 22 samples are prepared with the velocity controlled dip-coating setup in solutions of 15mg of C32 disolved in 20ml of C7 and studied immediately after dipping with SEM. The first samples shown in this work demonstrate the

velocity dependence of the generated structures. These samples are ST008 and ST011 and each one these is withdrawn at two different velocities, ~ 3 cm/min and 1 cm/min, to investigate the velocity dependence. At ~ 3 cm/min we see the formation of stripes of material spaced by nearly 8μm. Then a slow transition from stripes to dragon fly structures is seen as we advance to the region where the 1 cm/min withdrawing velocity stabilizes. We find that the stripes form parallel to the pulling direction, in contrast to the stripes found by M. Ghosh *et al.* [15]; although, some ideas from his work are used here to explain the growth mechanism of our submonolayer films. The dragon fly structures found in these 2 samples are anisotropic, growing larger in the direction opposite to the pulling of the substrate. From these two samples we obtain very similar results, finding a transition from stripe structures to dragon fly structures when two different withdrawal velocities are used on a same sample. This results confirms the velocity dependence of the structures that are generated with our velocity controlled dip-coating experiment.

With samples ST008 and ST011, the withdrawal velocity dependence of the submonolayer film is demonstrated, but a further rigorous study of the generated structures is also performed. The coverage and morphology of the generated structures is studied in a group of 8 samples, withdrawn each with a single velocity. The withdrawal velocities of the samples is varied from 0.2 cm/min to 6 cm/min.

Coverage versus withdrawal velocity plots are first shown. In these plots we can see that between 0.2 cm/min and 0.5 cm/min we observe an abrupt fall in coverage. We relate this to the transition from a gravity driven film growth to an entrained film regime proposed by M. Ghosh *et al.*[15], although slower withdrawal velocities would be required to prove this rigorously. The coverage has a minimum around 1 cm/min and for velocities above 1 cm/min we see a continuous rise in coverage. We relate this rise to the growth of the entrained C7 film thickness. As this film thickens with velocity, as predicted by L.D. Landau *et al.* [22], the coverage rises. This is an evidence that the solution is made of micrometer sized bulk C32 crystals with a determined size distribution. If the solution was made of individual molecules this coverage dependence above 1 cm/min would not be seen. As the entrained films thickens more bulk crystals

enter the precursor C7 film pinning to the substrate near the contact line. In this case, we should expect that the coverage reaches a maximum for velocities higher than 6 cm/min. This is also an open research topic.

The morphology of the generated structures is studied next, as a function of withdrawal velocity using two measurements: the isotropy and the subfinger instability length. The isotropy of the formed structures is studied defining a parameter α, that is the ratio between the finger that grows in the pulling direction and the finger that grows in the opposite direction. We see in the plot of α versus withdrawal velocity, that the isotropy presents a maximum around 1.5 cm/min where $\alpha \sim 0.5$; and approaches cero as the velocity is raised. At 6 cm/min, sample ST020, we see that our dragon fly structures tend to stretch enormously against the pulling direction, forming stripes of material. These stripes are much thinner the ones seen in sample ST008 and ST011 that were pulled in the stripe region at $\sim$ 3 cm/min. Samples between 3 cm/min and 6 cm/min have not been prepared and it is left as an open work to see how the width and periodicity of the stripe structures depend on velocity. Nevertheless we have been able to determine the velocity range in which these stripes are formed.

The instability length of the subfingers that grow in our dragon fly structures is also measured and plotted against withdrawal velocity. We find that this length decays exponentially. In fact, this decay can be fitted by a sum of two exponential functions. This is further evidence that we are in presence of two regimes of film growth.

Finally, thermal stability checks are performed on the ST family of samples. Sample ST006 (U = 1 cm/min) and ST005 (U = 0.2 cm/min) were imaged, using SEM, four months after preparation. We see that the dragon fly structures have slowly aggregated into bulk crystals of material. This indicates that even in ambient condition the molecules have a certain degree of mobility and that these dragon fly structure are not the energetically most convenient morphology.

The final sample presented is PM001, which is withdrawn at U = 1 cm/min. Immediately after preparation this sample was imaged with SEM. After this, a temperature

cycle is performed on this sample. This cycle goes from room temperature to the C32 first perpendicular layer melting temperature and then is cooled down again. After this cycle the sample is imaged again using SEM. We can see from these images that the original dragon fly structures turn into seaweed like figures. These shapes are typical of diffusion limited aggregation growth (DLA), where particles aggregate on a central seed from a disordered liquid melt. Furthermore, fractal analysis is done on this seaweed shape using the box-counting method. The fractal dimension obtained is D=1.71, which is a typical fractal dimension associated to DLA growth and is also obtained in other studies with C30 [25]. This is further support to the idea that our C7 solution is composed by micrometer sized bulk crystals of C32. If this solution were composed by single individual molecules, the final structures would look more like these seaweed isotropic structures typicall of DLA.

Our final conclusion is that dragon fly structures are formed by micrometer sized bulk crystals of C32 that pin to the substrate near the contact line. As the contact line retrocedes it layers the bulk C32 crystal into a well defined submonolayer structure, such as dragon flies or stripes. This is why we cannot see bulk particles immediately after dipping the sample. We believe to have important evidence that these submonolayer coverage structures are product of the combined effect of the silicon surface adhesion and the retroceding C7 contact line. Furthermore, the morphology of these structures can be controlled by varying the withdrawal velocity, from dragon fly structures to stripes of first perpendicular layers of material.

Future works should focus on the velocity ranges that have not been studied here. Such velocities are, for example, the range below 0.2 cm/min and between 3 cm/min and 6 cm/min. This last range is the most important, from an application point of view, because we believe that stripe structures are formed here; and furthermore, their width and periodicity could be controlled by the withdrawal velocity. The future importance of this work is related to the possibility of micro-structuring energetically homogenous surfaces, like silicon, with nanometer thick films using the relatively simple dip-coating procedure. These micro-structured patterns or stripes could be applied as optical diffraction grids or as templates for other materials.

Bibliography

[1] Vollhardt K., Schore N., *Organic Chemistry Structure and Function*, W.H. Freeman and Company, Third Edition 1999.

[2] Gedde U.W., *Polymer Physics*, Kluwer Academic Publishers, First Edition 1995.

[3] Lamoreaux S.K, *Casimir forces: Still surprising after 60 years*, Physics Today, Febuary 2007, p.40-45.

[4] M.P. Seah, S.J. Spencer: J. Vac. Sci. Technolog. A 21 (2003) 345-352.

[5] U.G Volkamnn, M. Pino, L.A. Altamirano, H. Taub, F.Y. Hansen, J. Chem. Phys. 116, 2107 (2002).

[6] S. Trogisch, M.J. Simpson, H. Taub, U.G. Volkmann, M. Pino, F.Y. Hansen. J. Chem. Phys. 123, 154703 (2005).

[7] H. Mo, S. Trogisch, H. Taub, S. N. Ehrlich, U. G. Volkmann, F. Y. Hansen and M. Pino. Phys. Stat. Sol. 201, 2375-2380 (2004).

[8] H.Mo, H. Taub, U.G. Volkmann, M. Pino, S.N. Ehrlich. F.Y. Hansen, E. Lu, P. Miceli, Chem. Phys. Lett. 377 (2003), 99-105.

[9] M.Bai, S.Trogisch, S. Magonov, H. Taub, Ultramicroscopy 108 (2008) 946-952.

[10] M. Bai, K. Knorr, M.J. Simpson, S. Trogisch, H. Taub, S.N. Ehrlich, H. Mo, U.G. Volkmann, F.Y. Hansen, EPL 79 (2007) 26003.

[11] "Flow Induced Growth of Striped Alkane Monolayers", M. Bai, H. Taub, A. Diama, K. Knorr, U. Volkmann,F. Hansen, APS 2008 (Oral Session).

[12] Joannopoulos, J.D.; Villeneuve, P.R.; Fan, S.H. Nature 1997, 386, 143.

[13] Holtz, J.H.; Asher,S.A. Nature 1997, 389, 829.

[14] Velev, O.D.; Jede, T.A.; Lobo, R.F.; Lenhoff,A.M. Nature 1997,389 447.

[15] M. Ghosh, F. Fan, K.J. Stebe, Langmuir, Vol. 23, No. 4, 2007.

[16] "Design with PIC Microcontrollers", John B. Peatmaan, 1998 Prentice Hall.

[17] "Atomic Force Microscopy, Scanning Nearfield Optical Microscopy and Nanoscatching Application to Rough and Natural Surfaces", G. Kaupp © Springer-Verlag Berlin Heildelberg 2006.

[18] G. Binning, C.F. Quate, Ch. Gerber, Phys. Rev. Lett. Vol. 56 No. 9 (1986).

[19] "Atomic Force Micrsocopy for Biologists", V.J. Morris, A.R. Kirby, A.P. Gunning © 1999 by Imperial College Press.

[20] "Scanning Electron Microscopy and X-Ray Microanalysis", J. Goldstein *et al.*, 3rd edition Springer 2003.

[21] "Scanning Electron Microscopy Physics of Image Formation and Microanalysis", L. Reimer, 2nd edition Spinger-Verlag Berlin Heilelberg New York.

[22] Landau L.D, V.G. Levich, Acta Physicochimica URSS,17, 42-54 (1948).

[23] A. Holzwart, S. Leporatti and H. Riegler, EPL 52 (6), pp.653-659 (2000).

[24] R. Köhler, P. Lazar, and H. Riegler, Appl. Phys. Lett. 89, 241906 (2006).

[25] L. Knüfing, H. Schollmeyer, H. Riegler, and K. Mecke, Langmuir, Vol. 21, No. 3, 2005.

[26] "Fractals in the Physical Sciences", H. Takayasu, Chichester : Wiley, c1990.

[27] T.A. Witten, L.M. Sander, Phys. Rev. B Vol. 27, No. 9, 1983.

[28] J.S. Langer, Rev. Mod. Phys., Vol. 52, No. 1, Jan. 1980.